

Review

Emerging biomedical imaging-based companion diagnostics for precision medicine

Shiyi Liao,¹ Mengjie Zhou,¹ Youjuan Wang,¹ Chang Lu,¹ Baoli Yin,¹ Ying Zhang,¹ Huiyi Liu,¹ Xia Yin,¹ and Guosheng Song^{1,*}

SUMMARY

The tumor heterogeneity, which leads to individual variations in tumor microenvironments, causes poor prognoses and limits therapeutic response. Emerging technology such as companion diagnostics (CDx) detects biomarkers and monitors therapeutic responses, allowing identification of patients who would benefit most from treatment. However, currently, most US Food and Drug Administration-approved CDx tests are designed to detect biomarkers *in vitro* and *ex vivo*, making it difficult to dynamically report variations of targets *in vivo*. Various medical imaging techniques offer dynamic measurement of tumor heterogeneity and treatment response, complementing CDx tests. Imaging-based companion diagnostics allow for patient stratification for targeted medicines and identification of patient populations benefiting from alternative therapeutic methods. This review summarizes recent developments in molecular imaging for predicting and assessing responses to cancer therapies, as well as the various biomarkers used in imaging-based CDx tests. We hope this review provides informative insights into imaging-based companion diagnostics and advances precision medicine.

INTRODUCTION

With the growth of the population and the accentuation of the problem of aging, coupled with bad habits such as smoking, unbalanced diet, and lack of exercise, the occurrence of various diseases such as tumors and cardiovascular diseases is increasing year by year.^{1,2} At the same time, modern medical technology is also developing rapidly in parallel, leading to new discoveries and thus providing models improved health-care. To date, the therapeutic drug development models for every disease have tried to investigate the biochemical pathway involved in the pathogenesis of that condition. This has resulted in the invention of several drugs, beginning with the widely used “paracetamol,” which targets inflammatory pathways, and progressing to “antihistamines,” and the chemotherapeutic drugs that inhibit the DNA synthesis pathways.³ Although this pharmacotherapeutic strategy has greatly aided in the development of outstanding drugs and therapeutic models for a wide range of diseases, it has also encountered the considerable number of treatment failures. These failures have not been ignored, leading to increasingly targeted therapeutic methods, not for a group of patients with a specific disease, but for the individual.

Precision medicine with a focus on individuals has become a major goal of researchers and is regarded as the future of medical care.^{4–6} It is based on individual differences in genes, environment, work, and lifestyle and applied modern molecular biology,⁷ molecular pathologies,⁸ molecular genetics, molecular imaging technology,^{9–11} bio-information technology, and the current popular big data technology¹² and artificial intelligence technology¹³ to analyze patients’ living environment and clinical data to obtain accurate disease categorization and diagnosis, and to generate individualized disease preventive and treatment strategies. Precision medicine in clinical practice aims to reduce iatrogenic damage, medical expenses, and patient benefits by selecting and using suitable diagnosis and treatment procedures for each patient.^{14,15} An emerging technology is companion diagnostics (CDx) tests that can select those patients who can benefit from a particular treatment or monitor the therapeutic response by detecting specific biomarkers, which potentially address tumor heterogeneity and improve therapeutic outcomes. The objectives of companion diagnostic testing include identifying patients who responded to therapeutic product, identifying patients determined to be at high risk of serious adverse effects,¹⁶ with the use of the therapeutic product,

¹State Key Laboratory for Chemo, Biosensing and Chemometrics, College of Chemistry and Chemical Engineering, Hunan University, Changsha 410082, China

*Correspondence: songgs@hnu.edu.cn
<https://doi.org/10.1016/j.isci.2023.107277>



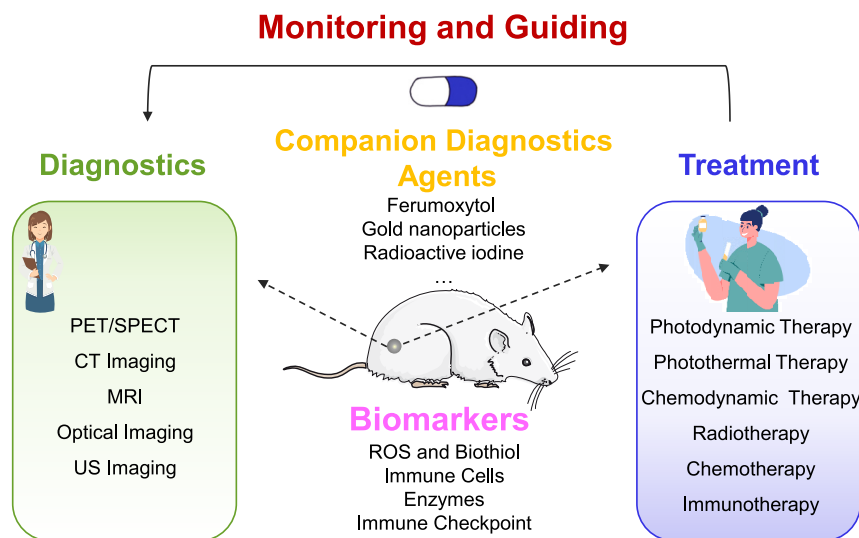


Figure 1. Schematic diagram showing the process of imaging-based companion diagnostics

monitoring the therapeutic effect of the therapeutic product and adjusting the duration, dose, or discontinuation of treatment to better achieve safety and efficacy; and identifying patients in the population who have determined that the therapeutic product is safe and effective for them.¹⁷ In 1998, the US Food and Drug Administration (FDA) approved the first companion diagnostic reagent, the HER2 test developed by Dako.¹⁸ To date, 43 kinds of companion diagnostic reagents have been approved by the FDA. Currently, most of FDA-approved CDx are adapted to testing the biomarkers *in vitro* and *ex vivo* (e.g. programmed death ligand 1 (PD-L1), tumor suppressor p53, or tyrosine protein kinase),¹⁹ using the established technologies (e.g. PCR, DNA sequencing, or immunohistochemistry). The tumor tissue or body fluids (including blood, urine, saliva, cerebrospinal fluid, semen, etc.) are required for biopsy to select patients or therapeutic target for treatment. It has been shown that patients who get a therapy that includes a companion diagnostic experience fewer grade 3 or 4 adverse responses and a lower incidence of treatment discontinuation, demonstrating the value of the information obtained from these tests.²⁰ However, *in vitro* companion diagnostics cannot determinate the location of tumors and small metastases of tumors. Also, *in vitro* companion diagnostics does not allow for real-time monitoring of treatment.

As a result, novel molecular-imaging-based CDx has been created to enable real-time tumors diagnosis and treatment response monitoring for precision medicine.²¹ The only imaging-based CDx currently authorized by the FDA is FerriScan, which enables a MRI assessment of iron concentration in liver of patients with nontransfusion-dependent thalassemia with treatment of deferasirox.²² Recently, the development of molecular imaging affords the ability to measure tumor heterogeneity and dynamically detect responses to treatment, for example, nuclear medicine techniques,^{23,24} ultrasound imaging,^{25,26} MRI,²⁷ computed tomography imaging (CT),^{28,29} or optical imaging^{30,31} to predicate therapeutic efficacy. Based on the importance of companion diagnostics in the development of precision medicine, we provide a brief overview of the molecular imaging paradigm developed in recent years, as well as innovative approaches to using molecular imaging to predict and assess response to cancer therapies (Figure 1). Meanwhile, we summarized the different types of biomarkers used in imaging-based companion diagnostics. We hope this review will provide some instructive perspectives on imaging-based companion diagnostics and promote the development of precision medicine.

DIFFERENT TYPES OF IMAGING FOR COMPANION DIAGNOSTICS

Molecular imaging is a relatively recent biomedical science that allows for the characterization, visualization, and measurement of biological processes at the cellular and subcellular levels within living people.³² Furthermore, because molecular and genetic changes occur before anatomic alterations during disease progression, molecular-genetic imaging can identify events that occur early in disease progression, such as carcinogenesis.³³ Several preclinical investigations in the development of imaging-based companion diagnostics for various imaging modalities were reported throughout the literature: positron emission

tomography (PET) or CT for investigating tumor accumulation of nanoparticles, MRI for monitoring drug release, second near-infrared region (NIR-II) fluorescence imaging for distinguishing patients suitable for glioblastoma (GBM) immunotherapy and photoacoustic imaging for early diagnosis of liver metastases and lung cancer, etc. This section provides an overview of current imaging-based companion diagnostics techniques, as well as their recent progress.

NUCLEAR MEDICINE TECHNIQUES

Compared to other imaging methods, nuclear medicine techniques such as PET and single-photon emission computed tomography (SPECT) offer incomparable detection sensitivity, allowing whole-body imaging to detect the levels of target molecules as well as the mutational status. Both PET and SPECT are more commonly used for imaging tumors and cardiac sites, while SPECT also has some other functional images such as kidney, bile, thyroid, stomach, bone disease, internal bleeding, and so on. In general, PET is currently used more for whole-body tumor screening and SPECT is used more for localized lesions. As a result, nuclear medicine imaging-based companion diagnostics may be beneficial to patients. New radiopharmaceuticals will enter clinical use as theranostics and companion diagnostics. Molecular imaging with different PET improved the ability to visualize tumors, metabolic activity, and other biological phenotypes (e.g., hypoxia,³⁴ proliferation,^{35,36} target receptors expression^{37,38}). What's more, a large number of new tracers may now be used in cancer clinical trials thanks to the widespread usage of noninvasive imaging techniques like PET/SPECT and gamma scintigraphy. For instance, tumor glycolytic activity and proliferation are monitored with ¹⁸F-FDG and ¹⁸F-FLT, while peptide compounds and antibodies labeled with technetium ^{99m}Tc- are frequently employed to identify cancer sites. In 2022, Mishiro and co-workers developed a ¹²⁵I-labeled osimertinib analog ([¹²⁵I]), and labeled this analog with ⁷⁷Br, ¹²⁵I, or corresponding nonradioactive compounds at its indole ring, respectively. Then, they used it for companion diagnosis for patients with non-small-cell lung cancer with the EGFR L858R/T790M double mutations (Figure 2A).³⁹ The findings demonstrate that osimertinib's affinity for the EGFR is unaffected significantly by halogenation at the indole's 5-position. The EGFR L858R/T790M double mutations can be particularly targeted by the probes with high activity *in vitro*. In biodistribution studies, tumors with mutations accumulated more [¹²⁵I] and [⁷⁷Br] than blood or muscle (Figure 2B). These results provide useful information for the development of practical concomitant diagnostics based on nuclear medicine techniques.

Nuclear medicine techniques have also been employed to study the accumulation of nanomedicines at tumor sites. Most passive targeting is based on enhanced permeability and retention effect (EPR) effects. In 2020, Goos and co-workers synthesized a star copolymer with 7–8 center-cross-linked arms. Then, they modified the arms with Gd³⁺ and ⁸⁹Zr for MRI and *in vivo* quantification and PET imaging, respectively (Figure 2C).⁴⁰ Tumors with low EPR characteristics (BxPC3) showed significantly lower uptake of the star polymers than tumors with low EPR characteristics (CT26), indicating passive tumor accumulation of the nano-stars through EPR effect (Figures 2D–2F). Meanwhile, the tumor growth rate was significantly more inhibited in mice treated with the high dose than in mice treated with the low dose, which demonstrates that EPR-based imaging can respond to treatment effects (Figure 2G). In order to examine the tumor accumulation in mice, Banerjee and co-workers radiolabeled both actively prostate-specific membrane antigen (PSMA)-targeted nanoparticles and their corresponding passively targeted controls (UNP) with indium-111 (¹¹¹In) (Figure 2H).⁴¹ As shown in Figure 2I and 48 h after injection, ¹¹¹In-labeled actively targeted nanoparticle levels accumulated to around 6% ID/g and stayed rather stable throughout time. ¹¹¹In-labeled untargeted nanoparticles, on the other hand, exhibited a greater tumor uptake of 8% ID/g at 48 h post-injection and a more pronounced clearance between 48 and 96 h. There are also strategies to modify the targeting moiety, such as fibroblast activation protein (FAP),⁴² somatostatin receptor,⁴³ and PSMA⁴⁴ on the tracers. For example, Zhong and co-workers synthesized [⁶⁸Ga]Ga-(FAPI-04)₂ using fibroblast activation protein inhibitor (FAPI).⁴² Micro-PET imaging of [⁶⁸Ga]Ga-(FAPI-04)₂ was done on SKOV3, A431, and H1299 tumor-bearing mice to evaluate tumor imaging and dimer retention time. [¹⁸F]F-FDG and [⁶⁸Ga]Ga-FAPI-04 were used for the control groups. The imaging data in all three tumor models revealed a fast absorption of [⁶⁸Ga]Ga-(FAPI-04)₂ by tumors following injection, with comparatively little uptake by other tissues and organs. The tumor-to-background ratios (TBRs) were elevated due to the quick clearance of uptake in normal tissues. Blockade imaging was conducted in A431 tumor-bearing mice to determine the binding specificity of the novel FAPI dimer to FAP. The results showed a significant reduction in radioactive uptake using unlabeled FAPI-04 monomer or DOTA-Suc-Lys-(FAPI-04)₂ as a competitive inhibitor. This design improved its retention time at the tumor site, and produced high-contrast imaging in xenografts after radionuclide labeling.

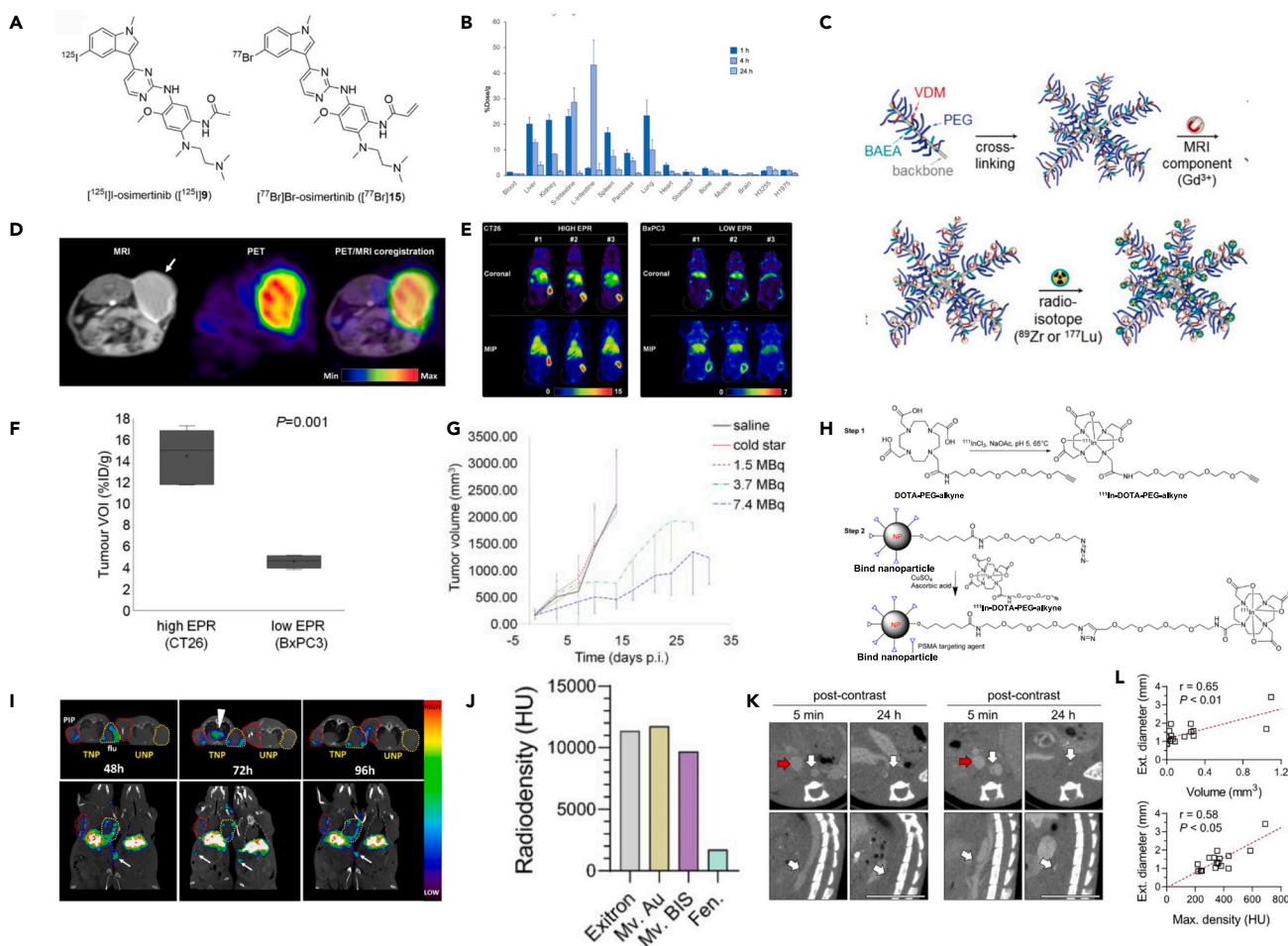


Figure 2. Graphs for companion diagnosis using PET or CT imaging

- (A) Structures of osimertinib analog labeled with $[^{125}\text{I}]$ or $[^{77}\text{Br}]$.
 (B) Biodistribution of radioactivity at 10 min, 1, 4, and 24 h after concomitant intravenous injection of $[^{77}\text{Br}]$ in H3255 and H1975 tumor-bearing mice.
 (C) Schematic representation of theranostic star polymer synthesis.
 (D) Enhanced T_1 -weighted contrast and PET images in BALB/c mice carrying CT26 tumors, after 3 days injection of nanostar.
 (E) Representative coronal and maximum intensity projection PET images of BALB/c mice carrying CT26 or BxPC3 tumors, 3 days after injection of ^{89}Zr -labeled nanostars.
 (F) Comparison of maximum uptake values in volumes of interest (VOIs) of CT26 and BxPCs tumors.
 (G) Tumor growth curves for each group treated with different doses of nanostar.
 (H) Two-step radiolabeling method for the PSMA-targeted nanoparticles.
 (I) Longitudinal *in vivo* SPECT-CT of ^{111}In -TNP and ^{111}In -UNP in xenograft-bearing mice.
 (J) Evaluation of four formulations of nanoparticle CT contrast.
 (K) Examples of CT images of mice at days 5–8 of Ang II infusion. Scale bar: 1 cm.
 (L) Correlation between nanoparticle enhancement volume (top) or maximal radiodensity (bottom) at day 5–8 and maximal external aortic diameter at 4 weeks.

CT imaging

CT is one of the most often utilized imaging techniques for cancer imaging in clinics due to its broad availability, fast imaging periods, and reasonably cheap cost. High atomic number nanoparticles with excellent X-ray attenuation, such as gold,⁴⁵ Gd,⁴⁶ iodine,⁴⁷ bismuth,⁴⁸ and ytterbium⁴⁹ nanoparticles can be used as CT contrast agents. To achieve tumor-specific uptake and delivery, encapsulation of these atoms into nanoparticles can be followed by functionalization to improve biocompatibility, prolong circulation half-life, and also coupling to the targeting fraction. Over the past two decades, a variety of nanoparticle contrast agents have been developed for X-ray imaging, such as gold nanoparticles for breast cancer imaging. However, in early work, imaging has not been used to reflect the results of treatment. In 2021, Toczek

et al. used the CT contrast nanoparticles to detect inflammation of the vessel wall *in vivo* by CT in abdominal aortic aneurysm (AAA) model mice (induced by angiotensin II (Ang II)). They firstly screened the most promising CT contrast agent Exitron nano 12000 (Figure 2J).⁵⁰ CT imaging in AAA model mice was used to analyze the biodistribution and uptake of nanoparticles in AAA. To investigate whether vessel wall CT enhancement correlates with AAA outcomes, a group of Ang II-infused Apoe^{-/-} mice were imaged with nanoparticle-enhanced CT within the first week of Ang II infusion, and their aortic external diameter and survival were assessed at 4 weeks. The nanoparticles aggregated inside the adventitia that had undergone remodeling, producing a CT signal that was linked with the expression of the macrophage marker CD68. Notably, the CT images taken within a week of the induction of AAA accurately predicted the outcome of AAA at four weeks, establishing a clear relationship between the degree of inflammation and AAA development.

Magnetic resonance imaging

Magnetic resonance imaging, as a noninvasive and nonionizing radiation imaging tool, may gather a range of information *in vivo*, such as molecular information, physiological processes, and anatomy information with excellent temporal and spatial resolution and great tissue penetration. Iron oxides have been widely used as an MRI contrast agent since 1978 when Ohgushi et al. first reported its ability to shorten the T₂ relaxation time of water and thus provided contrast.⁵¹ Due to the development of magnetic nanoparticles, magnetic imaging applications have substantially improved the capacity to monitor changes at the molecular level *in vivo*, which makes MRI practical for tumor detection, personalized treatment, tumor stratification, and other aspects.⁵²

Specifically, MRI-based techniques have been frequently used for drug release monitoring.⁵³ Since the interior of the nanocarrier is impermeable to water, the paramagnetic particles entrapped inside the nanocarrier induced only a slight T₁ shortening. However, when the nanocarrier ruptures and the paramagnetic particles released into an aqueous media, resulting in hyperintense signals in T₁-weighted MRI, this MRI signal change can then be used as a signal for drug release. As an example, Hennink et al. developed an MRI probe for monitoring drug release, consisting of temperature-sensitive liposomes (TSL) co-loaded with MR contrast agent ProHance (i.e., [Gd(HPDO₃A)(H₂O)]) and the doxorubicin (Figure 3A).⁵⁴ Meanwhile, NTSL (non-temperature-sensitive liposomes)-based probe was also synthesized for control experiments. At physiological temperature (T < T_m), unimpaird TSL and NTSL both showed no MRI contrast; when temperature increased (T > T_m), the lipid bilayer of the TSL re-arranged, leading to ProHance release and creating a dramatically enhanced MRI signal (Figure 3B). A strong association between the release of fluorescein and the release of contrast agent from TSL has been shown in this work (Figure 3C). In recent years, a range of strategies have also been developed for tumor microenvironment-specific release, where companion diagnostic reagents specifically respond to markers such as pH,⁵⁵⁻⁵⁷ hypoxia,^{58,59} reactive oxygen species (ROS),^{60,61} and biothiols⁶² to generate signal changes to assess drug release as well as therapeutic efficacy.

A second example of an MRI-based companion diagnostic approach relies on the accumulation of magnetic nanoparticles in tumors. In 2015, predicting therapeutic nanomedicine efficacy using a companion magnetic resonance imaging nanoparticle was reported by Miller and co-workers.⁵² They found that magnetic nanoparticles (MNP) uptake was positively correlated with the therapeutic effect of nanoparticles delivering chemotherapeutic drugs.

MRI can also provide information on tumor stratification. For example, in a recent report by Naumenko et al., a magnetic liposome (ML) consisted of ultrasmall citrate-coated MNP loaded into PEGylated liposomes was developed (Figure 3D).⁶³ The ΔSI value was calculated by imaging the 4T1 tumors before and 6 h after ML treatment, and 62 mice were divided into high and low accumulation subgroups. 18 mice with tumor ΔSI values above the median level and 13 mice with tumor ΔSI values below the median level were given the liposomal DXR (Caelyx), respectively, and the remaining animals were given the same dose of the non-encapsulated drug (Figures 3E and 3F). Compared to mice from the low accumulation group, animals with high ML uptake levels had more effective tumor growth inhibition and enhanced overall survival. Notably, Caelyx outperformed DXR in terms of therapeutic efficacy in animals with high ML uptake rates, but both drugs showed comparable antitumor effects in animals with low accumulation rates (Figures 3G and 3H). Overall, the overall conclusion is that the stratification of tumors according to companion MRI diagnostic may give chances for palliative therapy of patients with cancer, for example, when

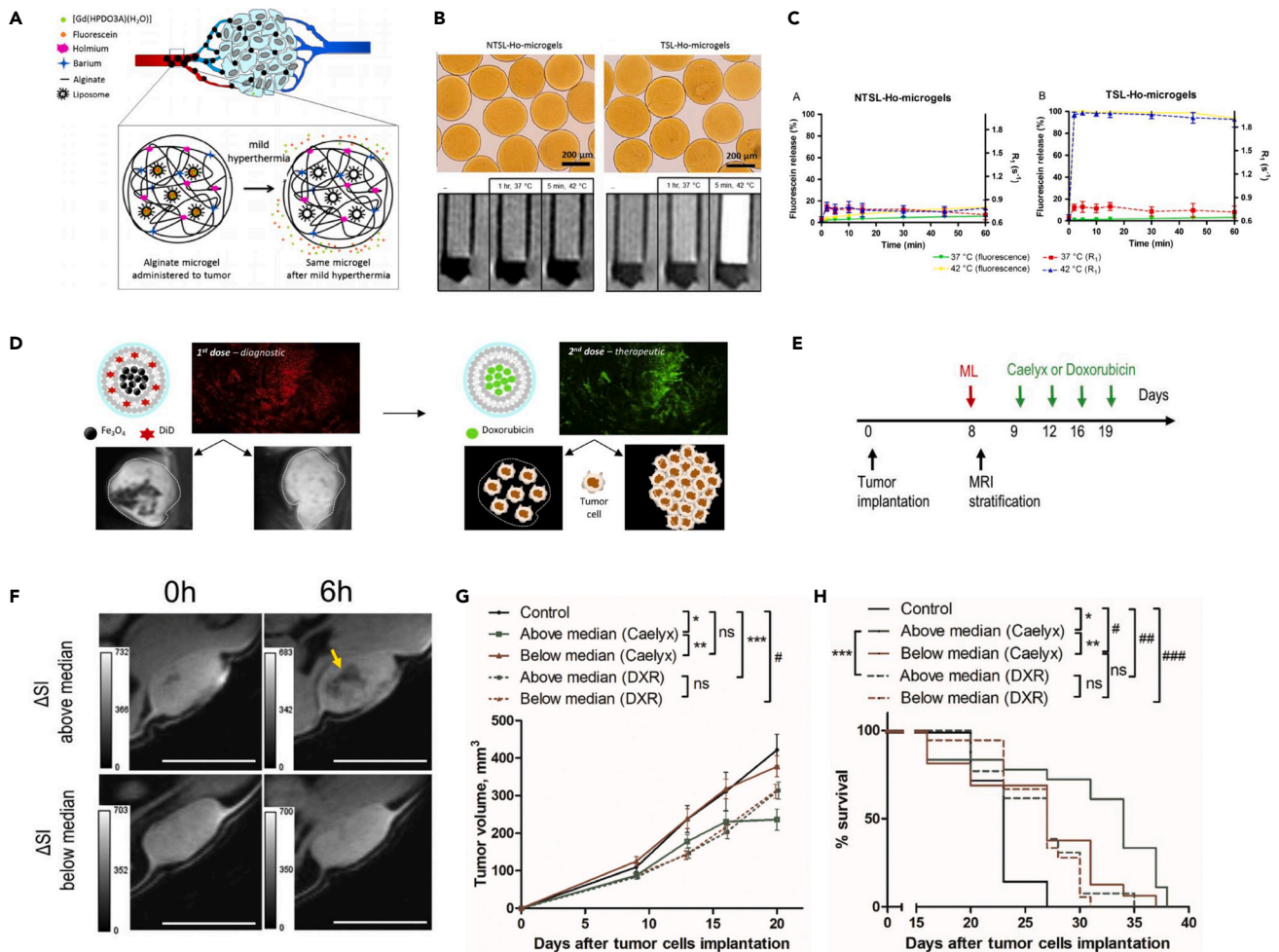


Figure 3. Graphs for companion diagnosis using MRI

(A) Schematic representation of accumulation of alginate microgels with encapsulated temperature-sensitive liposomes in a tumor during embolization. (B) Top: Light microscopy image of NTSL-Ho-microgels (left) and TSL-Ho-microgels (right) at room temperature. Bottom: T₁-wt MR images of NTSL-Ho-microgel (left) and TSL-Ho-microgel (right) dispersions at room temperature, after incubation at 37°C and 42°C. (C) T₂-wt MR images of a sheep kidney before (left) and after (right) the administration of TSL-Ho-microgels. (D) Illustration of liposomal companion diagnostic for cancer nanotherapy. (E) Experimental schedule for studying the prognostic value of ML in liposome-based cancer therapy. (F) Representative MR images of tumors with high and low ML deposition level. Scale bar, 5 mm. (G) Tumor measurements for 4T1-bearing PBS-injected mice (control) and animals treated with Caelyx or DXR. (H) Kaplan-Meier survival plots for the groups shown in (G).

tumors are too difficult to remove from patients or when antibody-based therapies are failing owing to acquired resistance.

Optical imaging

Near-infrared fluorescence imaging

For imaging-based CDx, near-infrared (NIR) optical imaging is the first choice thanks to its illustrious merits including noninvasiveness, low cost, zero radiation, hypotoxicity, portability, and the ability to provide real-time information.⁶⁴ NIR fluorescence imaging systems make use of a light spectrum with wavelengths greater than 650 nm. In this spectrum, autofluorescence is limited and intrinsic tissue's ability to absorb light—such as water and hemoglobin—is significantly diminished. As a result, it becomes possible to penetrate the tissues more deeply than with white light. Zhu and co-workers rationally designed and prepared M2-targeting Er-based NIR-IIb nanoprobes for GBM immunotherapy with little quenching effect and minimal overheating effect.⁶⁵ These probes exhibited downshifting fluorescence (1525 nm) and upconversion

fluorescence (540 nm) under 980 nm excitation, and can specifically identify M2-type tumor-associated macrophages (TAMs). After being functionalized by FAM-cys-M2pep (EDB-8.4 nanoparticles (NPs)), they demonstrated that the probes had good targeting ability *in vitro*. Afterward, orthotopic GBM NIR-IIb imaging and MRI were performed. They temporarily opened the blood–brain barrier (BBB) using focused ultrasound (FUS), then administered nanoprobe intravenously and obtained the NIR-II fluorescence images of brain. At 80 min post-injection, the TBR in GBM-bearing mice administered with EDBM-8.4 NPs peaked at 4.4, greater than that in animals administered with EDB-8.4 NPs (3.2). Moreover, the TBR of the active-targeting group mice was consistently higher than that of the nontargeted group mice, particularly at 120 min and 180 min post-injection. According to the findings, the dispersed M2-type TAMs in the tumor slices of mice that had been injected with EDBM-8.4 NPs were very consistent with the distribution of rare-earth ions (corresponding to brown dots). The synergistic effects of FUS therapy and M2pep polypeptide, which enabled effective enrichment and sustained retention of nanoprobe, may be responsible for the higher TBR. The outcome demonstrated that the NIR-IIb-targeted nanoprobe may be used as an NIR imaging-based CDx tool to discriminate between instances that respond to treatment and cases that do not respond to treatment as well as to evaluate the effectiveness of TAMs-based treatments.

Photoacoustic imaging

Photoacoustic (PA) imaging is of interest due to its ability to provide real-time imaging of tumors with deep tissue penetration and a high spatial resolution. The process of PA imaging is due to the fact that in biological tissues, PA agents convert the energy of short-pulsed laser generated by the PA imaging device into heat, which causes thermo-elastic expansion of tissues and brings about ultrasonic waves.^{66–68} PA imaging systems can detect and interpret these wideband acoustic waves, resulting in the generation of PA images. This comparatively novel imaging method has been applied to both organic and inorganic NPs. Upconversion NPs,⁶⁹ quantum dots,⁷⁰ inorganic NP frameworks of metals (particularly gold),⁷¹ other semiconductors,⁷² and polymers⁷³ have all been successfully utilized for preclinical visualization of cancer lesions, taking advantage of their natural NIR absorbance of these structures. In the study by Poon and colleagues, *ex vivo* tumors and organs from tumor-bearing mice were imaged using fluorescence and PA techniques with ultrasmall tiopronin-capped Au nanoparticles and the results were compared with inductively coupled plasma mass spectrometry (ICP-MS).⁷⁴ At the organ level, particle concentrations and distributions show good consistency. The localization of the particles within organ structures is made possible by spatial resolution from imaging techniques. Even though the particles lack a plasmon peak, their NIR absorbance is sufficient for PA excitation. When particle concentrations rise, PA imaging demonstrates an increase in signal along with spectral shifts as particles aggregate. Both of these imaging methods can shed light on particle distribution within cells and are noninvasive alternatives to ICP-MS. Also, responsive PA imaging companion diagnostic reagents have been developed. In 2022, Wu and co-workers reported a GOx-engineered conjugated polyaniline (PANI) nanoplatform (PANITG) for pH activatable, H₂O₂-responsive amplification of imaging-based CDx.²¹ To test the PANITG's potential for monitoring cancer treatment response, they performed PA imaging on mice injected with PANITG or PANI. Before the injections, due to the relatively low intrinsic tissue absorption in the NIR area, there was little PA signal detected inside the tumor. The PA signals of PANI and PANITG in tumor tissues steadily grew after the intravenous injection and peaked after 4 h of injection, when they were 2.0- and 2.9-fold greater than the background of tissue, respectively. The decrease in tumor pH leads to an increase in PA brightness, which indicates a better photothermal conversion, as evidenced by the tumor growth curve. Taken together, it was shown that the moderate acidity of the tumor “switched on” the PA signals of PANI and PANITG, but the signal strength of PANITG was further increased by the GOx catalytic process. To put it another way, PANITG's PA signal brightness might provide information on how the pH-activated and enhanced photothermal therapy (PTT) and the GOx-mediated starvation treatment are progressing, opening up the possibility for CDx.

Ultrasound molecular imaging

Ultrasound molecular imaging (USMI) uses microbubble ultrasound (US) contrast agents to provide functional and molecular imaging. US is a potent imaging tool due to its low spending, broad availability, non-radioactive, and real-time imaging capabilities.⁷⁵ Thanks to the discovery of ultrasonic contrast agents capable of targeting ligands such as antibodies or other proteins, ultrasound imaging has enabled molecular specificity, allowing the detection of cancer-specific molecular markers, such as B7-H3 (or CD276) in breast and ovarian cancer, or secreted frizzled-related protein 2 in angiosarcoma, for early detection of cancer, therapy response prediction, and treatment follow-up.^{75–77} For example, the *in vivo* vascular presentation of netrin-1 by endothelial cells in breast tumor models with netrin-1-positive is described by Wischhusen and colleagues (Figure 4A).⁷⁸ They also demonstrate the viability of ultrasound-based molecular imaging of netrin-1 to distinguish between high

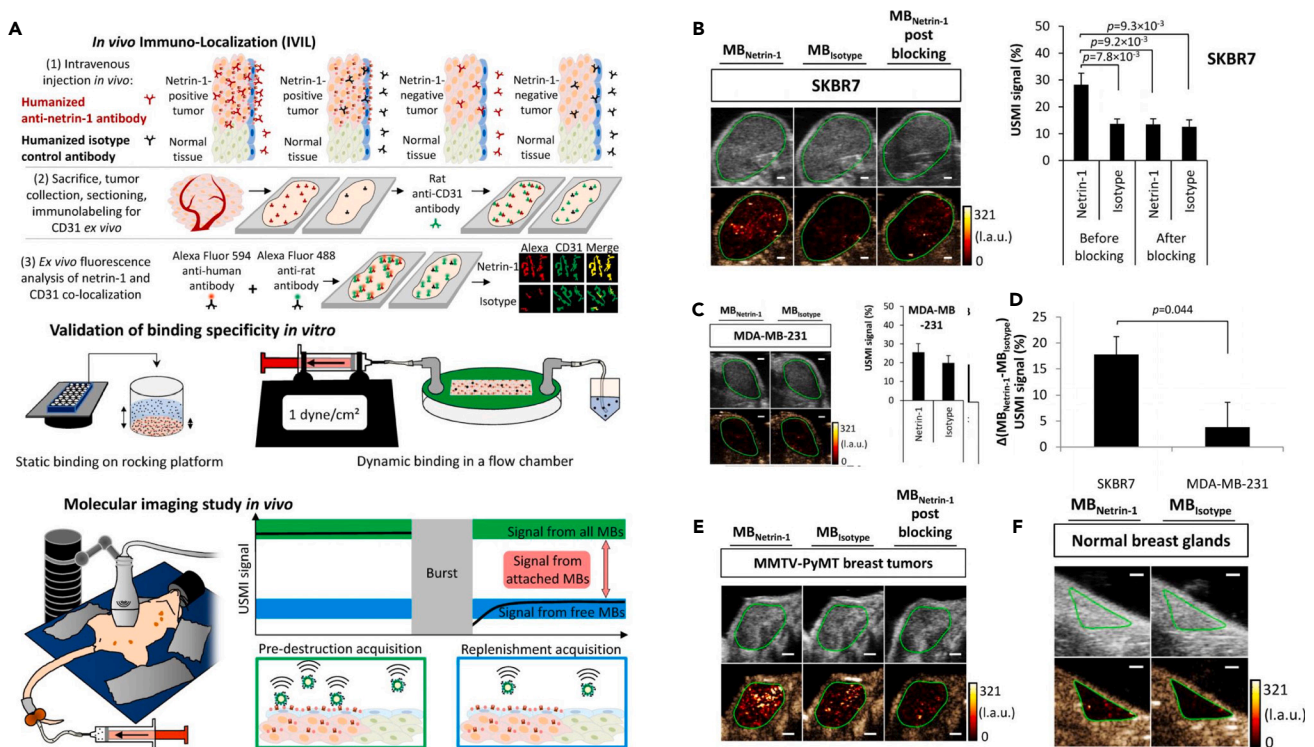


Figure 4. Graphs for companion diagnosis using ultrasound imaging

- (A) Illustration of *in vivo* immunolocalization analysis and imaging of netrin-1.
 (B) Netrin-1-positive human subcutaneous SKBR7 breast tumors in nude mice were imaged with both MB types prior to and post blocking with NET1-H-mAb.
 (C) Weakly netrin-1-expressing human subcutaneous MDA-MB-231 breast tumors were imaged with both MB types (N = 9).
 (D) The comparison of molecular imaging signal between SKBR7 tumors and MDA-MB-231 tumors.
 (E) USMI signal intensities obtained with anti-netrin-1-MBs (MB Netrin-1) and isotype control MBs (MB_{isotype}) prior to and post blocking of netrin-1 with NET1-H-mAb in MMTV breast cancer.
 (F) Imaging of normal mammary glands of wild-type mice with two types of MBs.
 Scale bars indicate 1 mm; error bars indicate SEM.

and low netrin-1-expressing tumors. They found that MMTV-PyMT mice and human breast tumor (strongly netrin-1-positive SKBR7)-bearing nude mice revealed an obviously increased signal with netrin-1-targeted microbubbles, while no discernible difference between control contrast agents and targeted in different types of mice models (Figures 4B–4F). The findings demonstrated that noninvasive, safe ultrasound molecular imaging could rapidly determine the level of netrin-1 expression. USMI may therefore develop into a companion diagnosis for patient stratification in upcoming clinical trials.

BIOMARKERS FOR COMPANION DIAGNOSTIC IMAGING

A one-size-fits-all approach to medical diagnosis and therapy can be impacted and improved by the use of imaging biomarkers in their many capacities. The use of biomarkers is fundamental to individualized oncology. Biomarker-based personalized oncology is already making a significant difference. Predictive, prognostic, and early-response biomarkers are three distinct categories of biomarkers that are particularly significant. Predictive biomarkers can address features of direct anticancer effectiveness specifically in oncology. Cancer prevention will be enhanced by tools for applying preventive medicine based on genetic and molecular diagnosis and therapies. In this section, we summarize biomarkers currently used for early diagnosis of diseases and therapeutic monitoring.

ROS and biothiols

GSH

Animals have an abundance of glutathione (GSH), a biological thiol that is crucial for detoxifying xenobiotics and maintaining redox equilibrium. Many diseases, including cancer, are linked to abnormal

alterations of GSH in the cellular levels. In comparison to healthy tissue, non-small-cell lung cancer has the greatest change in GSH levels. Importantly, GSH levels are elevated even at the onset of cancer, providing exciting opportunities for early cancer companion diagnostic. In 2021, Lucero and co-worker reported a photoacoustic imaging-based CDx probe (PACDx) for selective detection of GSH elevation in a lung cancer model.⁷⁹ Before activation, PACDx has very low absorption within the PA window (680–950 nm). Nevertheless, GSH treating causes a red shift. When PACDx was treated with GSH, a dose-dependent signal increase was seen with a limit of detection of 0.39 mM. Then, they attached gemcitabine to PACDx to form the gemcitabine-based prodrugs (herein named PARx). The *in vivo* results showed that PA signals were higher in PARx-treated tumors compared to control tumors. This suggests PARx activation, resulting in suppressed tumor growth. To assess the effectiveness of PACDx as a CDx, they created blind studies to explore whether the probe could pick out mice with lung cancer based on GSH levels from all experimental mice. First, a group of mice were implanted with either U87 (lowest GSH level) or A549 (highest GSH level) cells. The identity of the animals was kept secret until the study's conclusion after they had been tagged and randomly assigned by a second researcher. Instead of implanting no tumors, U87 cells were used to prevent any bias in the results caused by appearance. After the tumors reached a size of around 100 mm³, PACDx was given to perform PA imaging. The seven mice bearing different tumor types were stratified into two groups by PA imaging intensity. After prodrug therapy, it was shown that the group thought to have lung cancer did indeed react. It was gratified to find that the PACDx could precisely differentiate between various cancer kinds based on PA imaging when the identities of each animal were revealed. This study demonstrates the possible use of GSH as biomarkers and allows us to anticipate which group of animals will have the best therapeutic effectiveness when receiving therapy before treatment.

H₂O₂

ROS play a vital role in regulating physiological processes. Due to its stability under physiological conditions, hydrogen peroxide (H₂O₂) exists in the highest concentration (10⁻⁷–10⁻⁸ M range) among various ROS species.^{80,81} Normally, oxidative species generation is balanced by an innate antioxidant defense mechanism. A disruption in the redox balance, on the other hand, frequently causes the accumulation of H₂O₂, which can induce oxidative stress and damage to biomolecules. An elevated level of H₂O₂ is often used as a mark for various diseases, such as cancer, inflammation, and neurodegenerative disorders. Because of the important role of H₂O₂ in pathophysiology, imaging the distribution of H₂O₂ is essential for companion diagnostic and therapeutic applications. Therefore, efficient oxidative stress sensing probes suitable for preclinical and clinical models are in high demand. In Wu and co-workers' study, the pH-sensitive PANI nanoparticles are coupled to GOx via thiol-acetal compounds (TK), which are cleaved by H₂O₂ to form the so-called PANITG, which exhibits minimal NIR absorbance at physiological pH, but whose absorption profile turns red in more acidic environments. Thus, it is possible to distinguish diseased tissue from healthy tissue by "turning on" of PA signal in a mildly acidic tumor microenvironment. At the same time, transplanted GOx reacts with increased glucose in the tumor, leading to starvation of cancer and production of large amounts of glutamate and H₂O₂. They incubated the probes with 10 × 10⁻³ M glucose for 12 h. The H₂O₂ detected in the PANI solution (without GOx) was negligible, while a large amount of H₂O₂ was produced in the PANITG solution. The generated H₂O₂ led to the broken TK linkers and the intact GOx release. Subsequently, the released GOx was catalytic activity and able to produce even more H₂O₂ and glutamic acid, thus accelerating the cleavage process. They injected PANITG within the 4T1-xenografted tumor region and then recorded and analyzed the PA signal under laser irradiation at 680–970 nm. After subcutaneous injection, the PA signal in the tumor region increased significantly, with a peak at around 920 nm. Furthermore, the overproduction of glutamate during the catalytic self-amplification reaction due to increased local acidity contributes to enhanced PA and PTT imaging, and the increased PTT in turn contributes to the catalytic response. Additionally, since the processes occurring *in vivo* related to pH variation and GOx catalysis and can be reflected by the PA imaging brightness, it facilitates activated imaging-based CDx. Moreover, variations in oxygen saturation of oxygen-consuming hemoglobin during GOx catalysis were visualized *in vivo* by multiplex PA imaging, providing additional information for activated CDx in real time. Chen and co-workers constructed dual-mode NIR-II FL/PA ratio imaging nanoprobe (MTCNs) to achieve accurate and sensitive detection of H₂O₂ *in vivo*.⁸² They inoculated 4T1 cancer cells on the right hind footpad of mice and constructed a lymphatic metastasis tumor model to further evaluate the *in vivo* imaging performance of H₂O₂-responsive MTCN. The ratios of PA₈₀₈/PA₁₀₄₈ and FL_{1550Em,808Ex}/FL_{1080Em,980Ex} in sentinel lymph node (SLN) with metastasis were gradually increased and decreased, respectively, after the injection of MTCNs into the footpad of mouse. In contrast, healthy SLN showed no significant changes. The results demonstrate the

feasibility of using MTCNs as bimodal ratio imaging agents to accurately differentiate metastatic SLNs from non-metastatic SLNs according to their different H_2O_2 levels, for possible future use in companion diagnostic imaging.

Immune cells

Natural killer cells

Natural killer (NK) cells are innate lymphoid cells being explored because they participate in the tumor immune process by a different mechanism than T cells and could be exploited for treating people who do not respond to current immunotherapies.⁸³ Activated NK cells kill tumor cells by releasing cytoplasmic granules, death receptor-induced apoptosis, effector molecule production, or antibody-dependent cell-mediated cytotoxicity.⁸⁴ In addition, antigen presentation and uptake by DCs are improved by NK cells, enhancing antigen-specific cytotoxicity T lymphocytes responses. NK cells also produce cytokines to stimulate the activation of CD8⁺ T cells, such as interferon-gamma. Adoptive NK cell transfer therapy, used primarily in treatment of solid and hematological malignancies, is a treatment in clinical development involving *in vitro* stimulation and reinjection of the patient's own NK cells. Immune checkpoint inhibitors also apply their antitumor effects by activating NK cells. Thus, NK cell distribution during immunotherapy may serve as a valuable companion diagnostic imaging marker. Shaffer and co-workers developed L2 antibody-based PET probes specific for NKp30, an activation natural cytotoxicity receptor expressed by human NK cells.⁸⁵ The probes ^{64}Cu -NKp30Ab and ^{89}Zr -NKp30Ab showed specific binding in HeLa NKp30 cells, compared with both negative cells and isotype controls. Immunoreactivities of 72.3% for ^{64}Cu -NKp30Ab and 63.8% for ^{89}Zr -NKp30Ab were achieved (Figures 5A–5C). ^{64}Cu -NKp30Ab was further validated in both the human NK cell line NK92MI and human NK cells isolated from buffy coats and demonstrated specific *in vitro* binding (Figure 5D). Then, PET/CT and biodistribution results also demonstrated that NKp30 PET tracers labeled with ^{64}Cu or ^{89}Zr both demonstrated specificity *in vivo*, with ^{89}Zr -NKp30Ab exhibiting superior *in vivo* contrast at their respective optimal time points. To evaluate this tracer for imaging human NK cells *in vivo*, an ACT model was developed with NSG mice injected with NK92MI cells. In ACT mice at 48 h after injection, NSG mice injected with ^{64}Cu -NKp30Ab showed increased uptake in the spleen, and to a lesser extent the liver, compared with ^{64}Cu -IgG. In contrast, blood activity was lower for ^{64}Cu -NKp30Ab than for ^{64}Cu -IgG, likely because of increased ^{64}Cu -NKp30Ab uptake in the liver and spleen (Figure 5E). No other organs exhibited significant differences in ^{64}Cu uptake. The data support continued development of NK cell-specific PET tracers for imaging response during NK cell therapies that are currently being investigated in the clinic.

Tumor-infiltrating CD8⁺ T lymphocytes

Tumor-infiltrating CD8⁺ T lymphocytes are frequently considered as foundation of cancer immunotherapy since they exclusively recognize MHC I complex, an endogenous antigen peptide, and kill tumor cells. CD8⁺ T cells have been reported to have prognostic value in a variety of solid tumors, including gastric cancer, triple-negative breast cancer, colorectal cancer, melanoma, head and neck squamous cell carcinoma, liver cancer, and lung cancer.⁸⁶ Thus, clarifying the status and spatial distribution of CD8⁺ T cells *in vivo* by CDx holds immeasurable promise for application prospects in individualized cancer immunotherapy. Based on a collection of newly discovered nanobodies that target human CD8, Zhao and co-workers created ^{68}Ga -labeled tracers (^{68}Ga -NOTA-SNA006a) for immunoPET imaging of human CD8 antigen, which showed the good affinity, excellent pharmacokinetic characteristics, and targeting specificity (Figures 5F and 5G).⁸⁷ According to Figures 5H, ^{68}Ga -NOTA-SNA006a was only concentrated in the bladder and kidney of NPG and NSG control mice with a clear background. Significant uptake of CD8 tumors, spleen, lung, and liver tumors was observed in both hematopoietic stem cell (HSC)-NPG and PBMC-NSG mouse models, with higher uptake of CD8 tumors in HSC-NPG than in peripheral blood mononuclear cell (PBMC)-NSG. In contrast, PBMC-NSG model mice exhibited more uptake in spleen, liver, and lung. Flow cytometry and immunohistochemistry were used to confirm the expression of CD8 antigen in PBMC-NSG mouse model (Figure 5I). What's more, the results showed good correlation with the ^{68}Ga -NOTA-SNA006a immunoPET imaging results.

Tumor-associated macrophages

The macrophage-mediated innate immune response is one of the first lines to defend against invasion by various pathogens and inflammatory responses. TAMs are located around or inside and contribute to tumor progression and metastasis by a variety of mechanisms including angiogenic factor generation

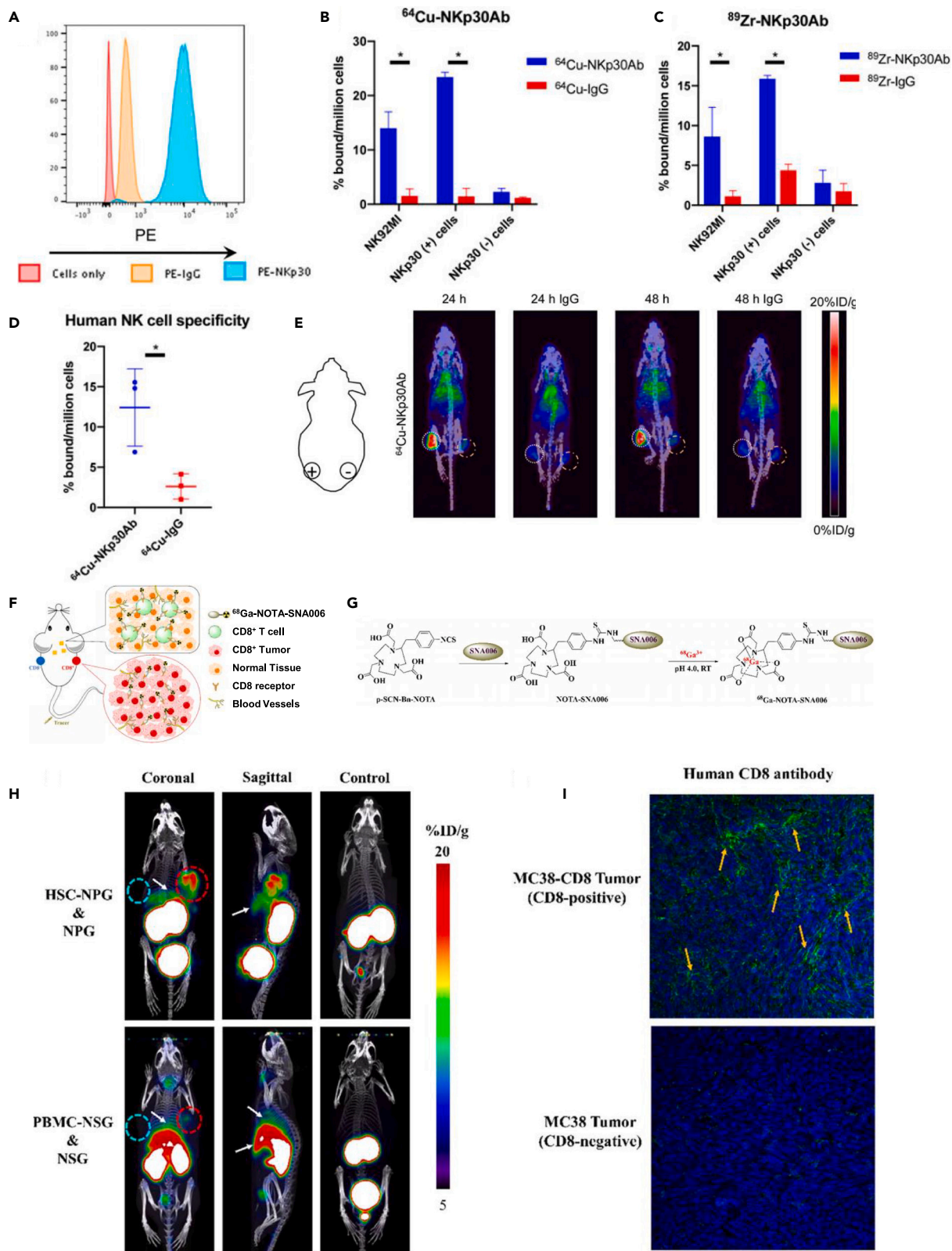


Figure 5. Graphs of NK cells or T cells as a companion diagnostic marker

- (A) Flow cytometry of NKp30-expressing HeLa cells.
- (B) Uptake of HeLa cells expressing NKp30 receptor NKp30-negative cell lines and NK92MI human NK cell line for ^{64}Cu -NKp30Ab.
- (C) Uptake of HeLa cells expressing NKp30 receptor NKp30-negative cell lines and NK92MI human NK cell line for ^{89}Zr -NKp30Ab.
- (D) Specific uptake of ^{64}Cu -NKp30Ab after 30 min incubation in isolated and *in vitro* activated human NK cells.
- (E) ^{64}Cu -NKp30Ab and ^{64}Cu -IgG PET/CT imaging of HeLa cell xenografts with (+) or without (-) NKp30-expressing at 24 and 48 h after injection.
- (F) Schematic illustration of ^{68}Ga -NOTA-SNA006 immunoPET in tracking CD8⁺ cells.
- (G) Synthetic scheme of ^{68}Ga -NOTA-SNA006.
- (H) The Micro-PET/CT imaging of ^{68}Ga -NOTA-SNA006a in HSC-NPG and PBMC-NSG mice models.
- (I) The human CD8 antigen immunohistochemical staining of tumors.

promoting angiogenesis or matrix disintegration. The phenotypes of M1 and M2 macrophages cooperate to promote tumor development.⁸⁸ Whereas M2 macrophages are anti-inflammatory and aid in the growth and progression of tumors, M1 macrophages are involved in inflammatory reactions, pathogen removal, and antitumor immunity. Therefore, it is essential for differentiate patients who are benefited from immunotherapies or to adjust treatment options in time to develop the imaging-based CDx to monitor TAMs. Zhu and co-workers developed Er-based nanoprobe for M2-type TAMs imaging in GBM using the NIR-II fluorescence. Er-based nanoparticles exhibit significant targeting ability to M2-type macrophages due to M2pep peptide functionalization. To explore the targeting ability of nanoprobe, they incubated EDBM-8.4 NPs with U87MG glioma cells and RAW264.7 cells for 2 h and found that M2-type macrophages endocytosed more EDBM-8.4 NPs than M1-type macrophages and U87MG glioma cells. After temporarily opening the BBB with FUS, the nanoprobe was then injected intravenously and NIR-II fluorescence images of the brain were collected. An intense fluorescence was immediately observed at the tumor site and gradually increased to a maximum 80 min after injection. In addition, due to the attached targeting peptide, the calculated TBR of mice in the active targeting group was consistently higher than that of the non-targeting group. The ability of these nanoprobe to target M2-type macrophages *in vivo* is also confirmed by overlaying immunofluorescence of M2-type TAM and staining with Arsenazo III rare-earth ions in tumor tissue. Tang's group⁸⁹ prepared a novel M2-like macrophage-targeting NO-responsive nanoprobe (NRP@M-PHCQ) through loading an NO-responsive NIR-II probe (denoted as NRP) into a polymer micelle made from an amphiphilic block polymer with mannose and hydroxychloroquine (HCQ) moieties (marked as M-PHCQ) for *in vivo* tracking M2-like macrophages and monitoring their polarization for *in vivo* tracking M2-like macrophages and monitoring their polarization. The mannose portion of the probe provides the ability to target macrophages. NRP@M-PHCQ facilitates early tumor metastasis imaging with high sensitivity and specificity by tracking M2-like macrophages *in vivo* and monitoring their polarization. They conducted *in vivo* imaging experiments using subcutaneous 4 T1 tumor, lymph node metastatic tumor, and lung metastatic tumor models. The tumor region of the NRP@M-PHCQ group gradually becomes brighter, but the NRP@M-PHCQ group's brightness was much lower than that of the NRP@M-PHCQ group's. Moreover, the groups with macrophage depletion had a considerable decrease in fluorescence intensity. These nanoprobe are intended to serve as a CDx agent to dynamically visualize the TAMs.

Enzyme

Nitroreductases

Nitroreductases (NTR) are a class of bacterial enzymes employed in GDEPT (gene-directed enzyme prodrug therapy) that preferentially activate aromatic nitro group-containing prodrugs to exhibit lethal effects in malignancies after gene transduction. The absence of translational imaging methods to measure drug cytotoxicity and gene transduction noninvasively has delayed the clinical development of NTR-based GDEPT. Garibay and co-workers developed a PET tracer for nitroreductases by radiolabeled 2-nitroimidazoles (2-NI).⁹⁰ Hypoxia promotes expression of nitroreductases, which is oxygen-sensitive and is capable of converting 2-NI (such as FMISO) into the corresponding hydroxylamines (Figure 6A). These hydroxylamines can covalently attach to macromolecules in the tumor and allow PET contrast. The results showed that PET contrast of ^{18}F -FMISO was significantly higher in NTR+ subcutaneous xenografts than in NTR-xenografts. Significant ^{18}F -FMISO retention was seen in orthotopic xenograft metastases (Figures 6B–6D). What's more, they reported the therapeutic effect of CB1954 in NTR-pressing xenografts using PET/CT imaging of ^{18}F -FMISO. There was a significant decrease in standardized uptake values in the CB1954 treatment group compared to the control group, consistent with a decrease in tumor size

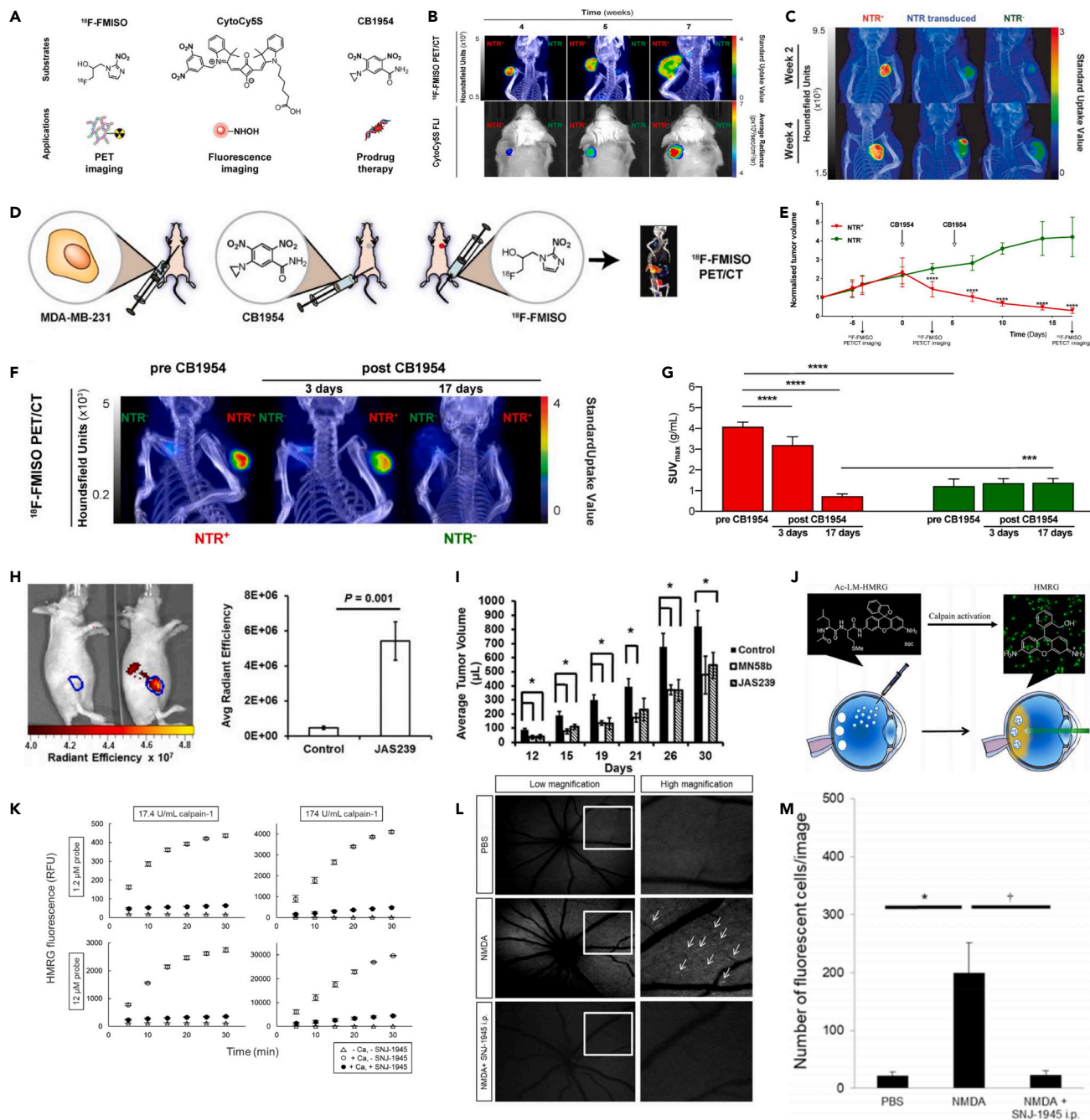


Figure 6. Graphs of enzymes as a companion diagnostic marker

(A) Nitroreductase substrates employed in imaging or GDEPT.

(B) Representative ^{18}F -FMISO PET/CT MIP images and CytoCy5S-FLI 2D surface weighted images over four weeks.

(C) Representative ^{18}F -FMISO PET/CT MIP images suggesting the expression of NTR in the *in vivo* transduced tumors both at week two and four after transduction.

(D) Experimental set-up for treatment monitoring employing ^{18}F -FMISO PET/CT imaging.

(E) Tumor growth curves of CB1954 treatment.

(F) Representative ^{18}F -FMISO PET/CT MIP images from NTR-tumor (left flank) and NTR+ tumor (right flank) before treatment and three and 17 days after CB1954 dosing.

(G) Before treatment, the SUVmax values before and after treatment.

(H) NIRF images and the quantitation of in vehicle-injected mouse (left) and mouse injected with JAS239 (right).

(I) Treatment for 5 consecutive days with MN58b or JAS239.

Figure 6. Continued

(J) Illustration of fluorescent probe of calpain.

(K) Ac-LM-HMRG hydrolysis by calpain-1.

(L) Real-time imaging of HMRG-positive cells after NMDA injury in rats that received SNJ-1945 or CMC intraperitoneally. White arrows show HMRG-positive cells.

(M) Quantitative data on the number of HMRG-positive cells in the real-time images.

(Figures 6E–6G). Their preclinical findings support the translational development of ¹⁸F-FMISO PET/CT for evaluating prodrug effectiveness in the background of NTR-based GDEPT.

Choline kinase alpha

Choline kinase alpha (ChoK), which is involved in the phosphorylation of free choline during cell entry or release by a catabolic process, is thought to be an important mediator of phosphorylcholine (PC) levels in cancer cells. The increase in intracellular PC during Ras transformation is a ChoK-dependent process, and ChoK inhibitors have been shown to block these changes. Choline kinase alpha expression is regarded as an important marker of breast cancer prognosis. The mechanism of involvement of this enzyme in the malignant transformation of tumors has been explored through the development of ChoK α inhibitors, but *in vivo* validation of specificity of this enzyme is difficult. Therefore, imaging-based companion diagnostic strategies have been developed to report the expression of this enzyme. Arlaukas et al. report optical imaging with JAS239, a carbocyanine-based ChoK α inhibitor with intrinsic NIR fluorescence, to assess the intracellular and natural state of ChoK α .^{91,92} Intracellular retention of JAS239 was suppressed by antibody blockade, suggesting that it interacts directly with ChoK α , independent of the choline transporter and cholinergic signaling pathways. Optical imaging of JAS239 in mice bearing orthotopic MCF7 breast xenografts allowed us to distinguish ChoK α -overexpressing tumors from tumors with empty carriers and to delineate tumor margins (Figure 6H). Pharmacological inhibition of ChoK with the known inhibitor MN58b suppressed the growth of 4175-Luc+ tumors, reduced the uptake of JAS239, and decreased the levels of total choline metabolites measured by magnetic resonance spectroscopy. When treated with higher therapeutic doses, JAS239 was as effective as MN58b in blocking MDA-MB-231 tumor growth and inducing apoptosis, and tumor choline levels were significantly reduced below baseline (Figure 6I). These results represent a novel approach to monitor the therapeutic potential of choline metabolism inhibition in breast cancer by small-molecule diagnostic approach.

Calpain

Calpain, a cysteine protease, is activated when intracellular calcium ions rise. Calpain activation contributes significantly to the process of retinal ganglion cell (RGC) death. RGC degeneration and death are significant events because they constitute the primary pathogenic alterations in numerous major blindness-causing disorders, including glaucoma and diabetic retinopathy. In a variety of clinical situations, local calpain activation via these calcium channels results in cell death. Calpain activation may play a role in a number of retinal illnesses in the central nervous system's visual system. As a result, blocking the calpain pathway has been researched as a promising treatment for these conditions. Toshifumi Asano and co-worker developed a new fluorescent probe and then used it in conjunction with a companion diagnostic system to monitor *in vivo* calpain activation (Figures 6J and 6K).⁹³ They firstly performed calpain-activated cell imaging in real time using Ac-LM-HMRG and performed cell counting with an injury model in rat retinas (induced by N-methyl-D-aspartate (NMDA)). More fluorescent cells were observed in the retinas treated with 20 μ M Ac-LM-HMRG after NMDA administration than that of PBS administration (Figure 6L). Quantitative data revealed that the group that received NMDA injections had a much larger number of fluorescing cells in comparison to the group that received PBS injections. Moreover, SNJ-1945 administered intraperitoneally dramatically reduced the quantity of fluorescing cells (Figure 6M).

Immune checkpoint

PD-L1

Immune checkpoint inhibitor medications that target the programmed death 1 (PD-1)/PD-L1 pathway are now standard of care in oncology. The binding of PD-L1 to PD-1 primarily occurs largely in inflammatory tissues and in the tumor microenvironment, where it leads to T cell downregulation and decreased immunity. By blocking PD-1 or PD-L1, cytotoxic T cells with specificity for cancer cells were preferentially activated. PD-L1 immunohistochemistry (IHC) 22C3 pharmDx is an FDA-approved companion diagnostic assay designed for the detection of PD-L1 protein.⁹⁴ However, the accuracy of the pathologic assessments as well

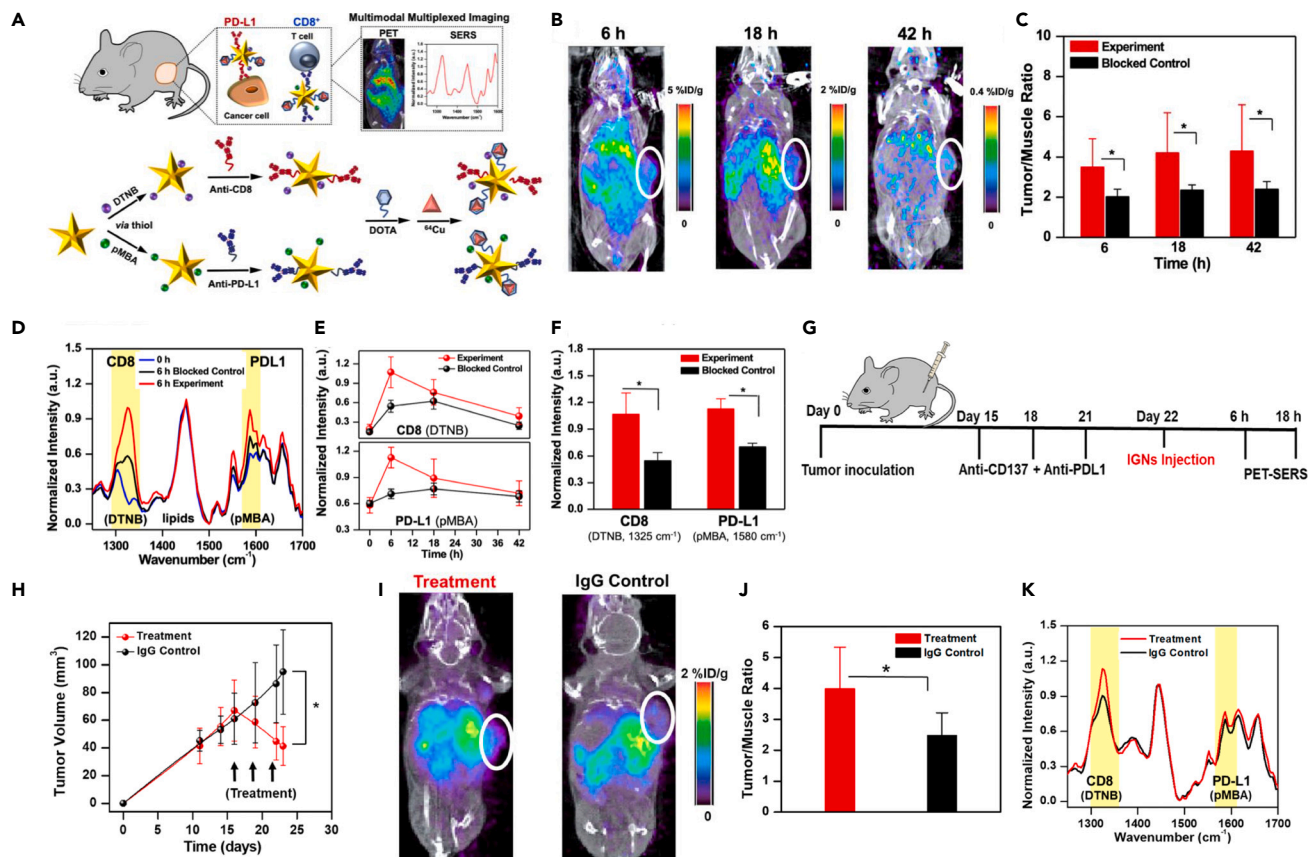


Figure 7. Graphs of PD-L1 as a companion diagnostic marker

(A) Schematic representation of IGMediated multimodal multiplexed ImmunoPET-SERS imaging to detect both PD-L1 expression and CD8⁺ T cells in melanoma tumors.
 (B) Whole-body PET/CT images of mouse bearing YUMM 2.1 tumors at 6, 18, and 42 h post-IGN delivery.
 (C) Longitudinal PET by examining tumor to muscle (T/M) ratio.
 (D) Normalized SERS spectra of tumors before IGMediated delivery (0 h) and at maximum accumulation time (6 h) of experimental and blocked control mice.
 (E) Longitudinal SERS analysis where pMBA and DTNB peaks were normalized to the intrinsic lipid peak at 1440 cm⁻¹.
 (F) SERS quantification of PD-L1 and CD8 at maximum accumulation.
 (G) Experimental procedure of imaging of mice bearing YUMM 2.1 tumors.
 (H) Tumor volumes decreased with immunotherapy.
 (I) PET-CT images of mouse revealed a higher localization of IGNs in tumors of treatment group (0.58% ID/g) relative to IgG control.
 (J) Corresponding PET quantification showing statistically significant differences in tumor/muscle ratio between treatment and control groups.
 (K) Averaged SERS spectra of treatment and IgG control group.

as the quality of immunohistochemistry testing is required for reliable results on the status of PD-L1. Molecular imaging of PD-L1 provides a noninvasive, alternative, and whole-body technique that addresses the practical challenge associated with IHC and has the ability to visualize intra-/inter-tumoral heterogeneity. In 2018, Bensch et al. evaluated clinical response to treatment with PD-L1 blockade using ⁸⁹Zr-atezolizumab.⁹⁵ Ou and co-workers have developed immunoreactive gold nanostars (IGNs), which reliably detect CD8⁺ T cells and PD-L1⁺ tumor cells *in vivo*, overcoming the drawbacks of current techniques for immunomaging (Figure 7A).⁹⁶ Nanostars were covalently linking to anti-PD-L1 monoclonal antibodies (mAbs) and covalently linked to the Raman reporter *para*-mercaptobenzoic acid in order to detect PD-L1. Next, nanostars were conjugated to DOTA before being radiolabeled with ⁶⁴Cu. Using a similar procedure, nanostars conjugated with anti-CD8 mAbs, the Raman reporter DTNB (5,5-dithiobis(2-nitrobenzoic acid)), and ⁶⁴Cu that made detection of CD8 facilitated. First, CT and PET images were obtained by scanning the whole body of mice after IGMediated administration and it was given a depth-resolved view and highly sensitive of the IGNs localization in tumors. The quick decay of ⁶⁴Cu is reflected by the decrease of the PET signal (Figure 7B). The ratio of the tumor to the nearby muscle (T/M) is obtained to account for the degradation of

^{64}Cu (Figure 7C). The specificity of IGNs in immunomarker detection was proven in mice that were pre-blocked for both PD-L1 and CD8 by delivering a saturating dose of anti-PD-L1 and anti-CD8 mAbs. Longitudinal PET pictures of blocked control animals revealed lower signal in tumors, which is consistent with prior PET imaging investigations. In experimental mouse tumors, quantitative PET measurement of the T/M ratio revealed strong signal from blocked control animals. Immediately after PET, they succeeded in multiplex detection of SERS using two different Raman tags, allowing PD-L1 and CD8 to be delineated in tumors with high spatial and temporal resolution (Figures 7D–7F). They also demonstrated the utility of IGNs for monitoring response to immunotherapies and separating responders from non-responders as well as multiplexed detection of immunomarkers. First, mice with YUMM 2.1 tumors were given combined anti-CD137 and anti-PD-L1 therapeutic antibodies. IGNs were administered 24 h after treatment, and then PD-L1 and CD8 status was monitored after treatment with ImmunoPET-SERS (Figure 7G). There was a reduction in tumor volume suggesting that combinatorial immunotherapy was effective for YUMM 2.1 tumors when compared to control mice. The T/M ratios calculated from PET signal analysis of revealed SSD between treated and untreated animals (Figures 7H–7J). Multiplexed SERS analysis was used to determine if the observed PET intensities increase was due to infiltration of CD8⁺ T cells or changes in PD-L1, or both. SERS revealed (Figure 7K) CD8⁺ T cell proliferation in treated mice tumors, which agreed well with PET data and a tumor size reduction of treatment group. Early detection of immunomarkers in this study will enhance therapeutic outcomes for responders and hasten clinical choices for those seeking alternative therapy, and reduce toxicities and high costs associated with ineffective treatments for nonresponders.

SUMMARY AND OUTLOOK

In this review, we briefly review new methods developed in recent years to apply molecular imaging to predict and assess response to cancer therapies, including MRI, optical imaging, ultrasound imaging, and nuclear medicine techniques. Meanwhile, we summarize different types of markers (ROS and biothiols, immune cells, enzymes, and immune checkpoint) for imaging-based companion diagnosis.

Precision medicine is receiving more and more attention nowadays, and molecular imaging plays an important role as companion diagnostics in precision medicine. For personalized treatment, it is vital to accurately analyze the expression of biomarkers. Molecular imaging provides noninvasive systemic information and also shows the changes in the content of various biomarkers, the changes of immune cells, and the bio-distribution of targeted drugs at the immune checkpoint. However, current biomarkers, such as ROS or GSH, have limited clinical utility and limited role in treatment. Therefore, new biomarkers are urgently needed to be introduced into imaging-based companion diagnostics to improve patient stratification and reduce overtreatment. For example, enzymes directly related to apoptosis (caspase 3, caspase 9 ...),⁹⁷ various immune cells involved in the immunotherapeutic process (T cell, NK cell ...), or biomarkers associated with tumor metastasis (MMP,⁹⁸ VEGF⁹⁹ ...), etc. Investigators can also develop corresponding *in vivo* imaging-based companion diagnostic probes based on established companion diagnostic test targets *in vitro* or *ex vivo*.

Future companion diagnostics will heavily rely on noninvasive imaging. When compared to other imaging techniques used *in vivo*, MRI has the highest spatial resolution and can image the complete human body because of its significant penetration depth. However, its low sensitivity limits its application *in vivo*. Optical imaging is superior due to its ease of use and allows a sensitive response to biomolecules, resulting in highly targeted and specific imaging.¹⁰⁰ But fluorescent signals are subject to attenuation and scattering, so optical imaging using fluorescence is difficult to obtain signals from deep tissue. The above disadvantages of fluorescence imaging can be compensated for by photoacoustic imaging. US technology is a powerful imaging tool due to its widespread availability, real-time imaging capabilities, low cost, and lack of radiation exposure to patients. Though, ultrasound imaging is restricted to soft tissues and cannot be applied to lung or bone metastases. Whereas nuclear imaging offers significant advantages in quantitative imaging, and it is possible to do whole-body analysis even for humans. However, due to its always-ON feature, it is inferior for specific imaging (Table 1).⁷⁵

As seen previously, there are pros and downsides to each imaging method. It should be possible for multimodal imaging to make up for the drawbacks and boost the benefits of each modality. Multimodal imaging ought to allow for the simultaneous characterization, visualization, and quantification of biological processes. Additionally, for precision medicine in each patient, the combination of multimodal imaging and therapy would be most beneficial. Therefore, more multimodal imaging modalities need to be developed

Table 1. Summary of imaging modalities

Types of imaging	Advantages	Disadvantages
Nuclear medicine techniques	Highly sensitive Limitless depth penetration	High cost Always-on feature
CT imaging	High resolution Limitless depth penetration	Radioactivity
Magnetic resonance imaging	High resolution	Low sensitivity
Optical imaging	Ease of use Highly sensitive	Low-depth penetration
Ultrasound molecular imaging	Ease of use	Restricted to soft tissues

for companion diagnostics. However, the multimodal imaging technique generally has more sophisticated requirements for contrast agents and imaging instruments. To solve this problem, many multimodal imaging devices have now been developed, such as PET/CT, SPECT/CT, PET/MRI, and SPECT/MRI. In addition, incorporating different imaging units into the probe can certainly increase the complexity, especially for clinical translation. We can find suitable carriers that can stably deliver multiple contrast agents to the target location.¹⁰¹ In addition, some emerging imaging techniques such as afterglow imaging^{102,103} and magnetic particle imaging can be applied to companion diagnosis,^{104–106} which will bring a new perspective to the current imaging-based companion diagnosis.

For better application of imaging-based companion diagnostics, we can develop NPs as imaging-based CDx agents. As compared to small molecules, nanoparticles can give improved tumor accumulation, stability, and circulation times. We hope to maintain their structural uniformity (shape and size), surface charge, and consistent loading of any drug or imaging agents' payloads to provide the basis for successful translation of NPs for clinical use.²⁰ What's more, we can encapsulate the therapeutic agent and the contrast agent in a nanoparticle, which ensures that the contrast agent and the therapeutic agent are accumulated in the same part of the body. However, the problem that the doses of therapeutic drugs and contrast agents are usually different still needs to be addressed. As shown by productive early-stage clinical trials, NP-based imaging agents have already proven to have distinct advantages for the noninvasive visualization of cancer. We believe that this analysis will raise more awareness of the difficulties and possibilities for the continued advancement and clinical application of imaging-based companion diagnostics.

ACKNOWLEDGMENTS

This work was supported by the National Natural Science Foundation of China (grants U21A20287, 22234003, 21977027, 21974039), the Science and Technology Project of Hunan Province (2020RC3022; 2020SK2014), Shenzhen Science and Technology Program (JCYJ20210324140205013).

DECLARATION OF INTERESTS

The authors declare no competing interests.

REFERENCES

1. D'Esposito, V., Di Tolla, M.F., Lecce, M., Cavalli, F., Libutti, M., Misso, S., Cabaro, S., Ambrosio, M.R., Parascandolo, A., Covelli, B., et al. (2022). Lifestyle and Dietary Habits Affect Plasma Levels of Specific Cytokines in Healthy Subjects. *Front. Nutr.* 9, 913176. <https://doi.org/10.3389/fnut.2022.913176>.
2. Wang, Q., Zeng, A., Zhu, M., and Song, L. (2023). Dual inhibition of EGFR-VEGF: An effective approach to the treatment of advanced non-small cell lung cancer with EGFR mutation (Review). *Int. J. Oncol.* 62, 26. <https://doi.org/10.3892/ijo.2023.5474>.
3. Puranik, A.D., Kulkarni, H.R., and Baum, R.P. (2015). Companion Diagnostics and Molecular Imaging. *Cancer J.* 21, 213–217.
4. Fruhbeck, G., Kiortsis, D.N., and Catalan, V. (2018). Precision medicine: diagnosis and management of obesity. *The Lancet. Diabetes & endocrinology* 6, 164–166. [https://doi.org/10.1016/S2213-8587\(17\)30312-1](https://doi.org/10.1016/S2213-8587(17)30312-1).
5. Paranjape, S.M., and Mogayzel, P.J., Jr. (2018). Cystic fibrosis in the era of precision medicine. *Paediatr. Respir. Rev.* 25, 64–72. <https://doi.org/10.1016/j.prv.2017.03.001>.
6. Qin, Y., Geng, X., Sun, Y., Zhao, Y., Chai, W., Wang, X., and Wang, P. (2023). Ultrasound nanotheranostics: Toward precision medicine. *J. Contr. Release* 353, 105–124. <https://doi.org/10.1016/j.jconrel.2022.11.021>.
7. Small, A., and Wechalekar, M.D. (2020). Synovial biopsies in inflammatory arthritis: precision medicine in rheumatoid arthritis. *Expert Rev. Mol. Diagn.* 20, 315–325. <https://doi.org/10.1080/14737159.2020.1707671>.
8. Naimat, F., Fahrni, M.L., Purushothaman, S., Abdul Ghani, M.N., Chumnumwat, S., and Babar, Z.U.D. (2022). Community pharmacists' perceived value on precision medicine, desired training components, and exposure during pharmacy education: Malaysia's experience. *Front. Pharmacol.* 13, 978141. <https://doi.org/10.3389/fphar.2022.978141>.

9. Lu, Z.R., Laney, V., and Li, Y. (2022). Targeted Contrast Agents for Magnetic Resonance Molecular Imaging of Cancer. *Acc. Chem. Res.* 55, 2833–2847. <https://doi.org/10.1021/acs.accounts.2c00346>.
10. Kim, H., Kwak, G., Kim, K., Yoon, H.Y., and Kwon, I.C. (2019). Theranostic designs of biomaterials for precision medicine in cancer therapy. *Biomaterials* 213, 119207. <https://doi.org/10.1016/j.biomaterials.2019.05.018>.
11. Dammes, N., and Peer, D. (2020). Monoclonal antibody-based molecular imaging strategies and theranostic opportunities. *Theranostics* 10, 938–955. <https://doi.org/10.7150/thno.37443>.
12. Panayides, A.S., Pattichis, M.S., Leandrou, S., Pitris, C., Constantinidou, A., and Pattichis, C.S. (2019). Radiogenomics for Precision Medicine With a Big Data Analytics Perspective. *IEEE J. Biomed. Health Inform.* 23, 2063–2079. <https://doi.org/10.1109/JBHI.2018.2879381>.
13. Boniolo, F., Dorigatti, E., Ohnmacht, A.J., Saur, D., Schubert, B., and Menden, M.P. (2021). Artificial intelligence in early drug discovery enabling precision medicine. *Expert Opin. Drug Discov.* 16, 991–1007. <https://doi.org/10.1080/17460441.2021.1918096>.
14. Whitcomb, D.C. (2019). Primer on Precision Medicine for Complex Chronic Disorders. *Clin. Transl. Gastroenterol.* 10, e00067. <https://doi.org/10.14309/ctg.000000000000067>.
15. Khoury, J.D. (2016). The evolving potential of companion diagnostics. *Scand. J. Clin. Lab. Invest. Suppl.* 245, S22–S25. <https://doi.org/10.1080/00365513.2016.1206444>.
16. Jørgensen, J.T. (2016). Companion and Complementary Diagnostics: Clinical and Regulatory Perspectives. *Trends Cancer* 2, 706–712. <https://doi.org/10.1016/j.trecan.2016.10.013>.
17. Jørgensen, J.T., and Hersom, M. (2018). Clinical and Regulatory Aspects of Companion Diagnostic Development in Oncology. *Clin. Pharmacol. Ther.* 103, 999–1008. <https://doi.org/10.1002/cpt.955>.
18. Cobleigh, M.A., Vogel, C.L., Tripathy, D., Robert, N.J., Scholl, S., Fehrenbacher, L., Wolter, J.M., Paton, V., Shak, S., Lieberman, G., and Slamon, D.J. (1999). Multinational Study of the Efficacy and Safety of Humanized Anti-HER2 Monoclonal Antibody in Women Who Have HER2-Overexpressing Metastatic Breast Cancer That Has Progressed After Chemotherapy for Metastatic Disease. *J. Clin. Oncol.* 17, 2639–2648. <https://doi.org/10.1200/JCO.1999.17.9.2639>.
19. Dracopoli, N.C., and Boguski, M.S. (2017). The Evolution of Oncology Companion Diagnostics from Signal Transduction to Immuno-Oncology. *Trends Pharmacol. Sci.* 38, 41–54. <https://doi.org/10.1016/j.tips.2016.09.007>.
20. Ehlerding, E.B., Grodzinski, P., Cai, W., and Liu, C.H. (2018). Big Potential from Small Agents: Nanoparticles for Imaging-Based Companion Diagnostics. *ACS Nano* 12, 2106–2121. <https://doi.org/10.1021/acsnano.7b07252>.
21. Wu, J., Zhang, Y., Jiang, K., Wang, X., Blum, N.T., Zhang, J., Jiang, S., Lin, J., and Huang, P. (2022). Enzyme-Engineered Conjugated Polymer Nanoplatforam for Activatable Companion Diagnostics and Multistage Augmented Synergistic Therapy. *Adv. Mater.* 34, e2200062. <https://doi.org/10.1002/adma.202200062>.
22. St Pierre, T.G., El-Beshlawy, A., Elalfy, M., Al Jefri, A., Al Zir, K., Daar, S., Habr, D., Kriemler-Krahn, U., and Taher, A. (2014). Multicenter validation of spin-density projection-assisted R2-MRI for the noninvasive measurement of liver iron concentration. *Magn. Reson. Med.* 71, 2215–2223. <https://doi.org/10.1002/mrm.24854>.
23. Horsman, M.R., Mortensen, L.S., Petersen, J.B., Busk, M., and Overgaard, J. (2012). Imaging hypoxia to improve radiotherapy outcome. *Nat. Rev. Clin. Oncol.* 9, 674–687. <https://doi.org/10.1038/nrclinonc.2012.171>.
24. Khalil, M.M., Tremoleda, J.L., Bayomy, T.B., and Gsell, W. (2011). Molecular SPECT Imaging: An Overview. *Int. J. Mol. Imaging* 2011, 796025. <https://doi.org/10.1155/2011/796025>.
25. Gao, Y., Hernandez, C., Yuan, H.X., Lilly, J., Kota, P., Zhou, H., Wu, H., and Exner, A.A. (2017). Ultrasound molecular imaging of ovarian cancer with CA-125 targeted nanobubble contrast agents. *Nanomedicine* 13, 2159–2168. <https://doi.org/10.1016/j.nano.2017.06.001>.
26. Uemura, H., Sano, F., Nomiya, A., Yamamoto, T., Nakamura, M., Miyoshi, Y., Miki, K., Noguchi, K., Egawa, S., Homma, Y., and Kubota, Y. (2013). Usefulness of perflubutane microbubble-enhanced ultrasound in imaging and detection of prostate cancer: phase II multicenter clinical trial. *World J. Urol.* 31, 1123–1128. <https://doi.org/10.1007/s00345-012-0833-1>.
27. Dong, Z., Liang, P., Guan, G., Yin, B., Wang, Y., Yue, R., Zhang, X., and Song, G. (2022). Overcoming Hypoxia-Induced Ferroptosis Resistance via a (19) F/(1) H-MRI Traceable Core-Shell Nanostructure. *Angew. Chem.* 61, e202206074. <https://doi.org/10.1002/anie.202206074>.
28. Park, J.Y., Chang, Y., and Lee, G.H. (2015). Multi-Modal Imaging and Cancer Therapy Using Lanthanide Oxide Nanoparticles: Current Status and Perspectives. *Curr. Med. Chem.* 22, 569–581. <https://doi.org/10.2174/0929867322666141128162843>.
29. Cormode, D.P., Naha, P.C., and Fayad, Z.A. (2014). Nanoparticle contrast agents for computed tomography: a focus on micelles. *Contrast Media Mol. Imaging* 9, 37–52. <https://doi.org/10.1002/cmmi.1551>.
30. Chen, H., Yuan, Z., and Wu, C. (2015). Nanoparticle Probes for Structural and Functional Photoacoustic Molecular Tomography. *BioMed Res. Int.* 2015, 757101. <https://doi.org/10.1155/2015/757101>.
31. Cheng, X., Chai, Y., Xu, J., Wang, L., Wei, F., Xu, G., Sun, Y., Hu, Q., and Cen, Y. (2020). Enzyme cascade reaction-based ratiometric fluorescence probe for visual monitoring the activity of alkaline phosphatase. *Sensor. Actuator. B Chem.* 309, 127765. <https://doi.org/10.1016/j.snb.2020.127765>.
32. Meng, Y., Sun, J., Qv, N., Zhang, G., Yu, T., and Piao, H. (2020). Application of molecular imaging technology in tumor immunotherapy. *Cell. Immunol.* 348, 104039. <https://doi.org/10.1016/j.cellimm.2020.104039>.
33. Kang, J.H., and Chung, J.-K. (2008). Molecular-Genetic Imaging Based on Reporter Gene Expression. *J. Nucl. Med.* 49, 164S–179S. <https://doi.org/10.2967/jnumed.107.045955>.
34. Wilson, W.R., and Hay, M.P. (2011). Targeting hypoxia in cancer therapy. *Nat. Rev. Cancer* 11, 393–410. <https://doi.org/10.1038/nrc3064>.
35. Hoeben, B.A.W., Troost, E.G.C., Span, P.N., van Herpen, C.M.L., Bussink, J., Oyen, W.J.G., and Kaanders, J.H.A.M. (2013). 18F-FLT PET during radiotherapy or chemoradiotherapy in head and neck squamous cell carcinoma is an early predictor of outcome. *J. Nucl. Med.* 54, 532–540. <https://doi.org/10.2967/jnumed.112.105999>.
36. Soloviev, D., Lewis, D., Honess, D., and Aboagye, E. (2012). [(18)F]FLT: an imaging biomarker of tumour proliferation for assessment of tumour response to treatment. *Eur. J. Cancer* 48, 416–424. <https://doi.org/10.1016/j.ejca.2011.11.035>.
37. Takamura, Y., and Kakuta, H. (2021). In Vivo Receptor Visualization and Evaluation of Receptor Occupancy with Positron Emission Tomography. *J. Med. Chem.* 64, 5226–5251. <https://doi.org/10.1021/acs.jmedchem.0c01714>.
38. Veronese, M., Zanotti-Fregonara, P., Rizzo, G., Bertoldo, A., Innis, R.B., and Turkheimer, F.E. (2016). Measuring specific receptor binding of a PET radioligand in human brain without pharmacological blockade: The genomic plot. *Neuroimage* 130, 1–12. <https://doi.org/10.1016/j.neuroimage.2016.01.058>.
39. Mishiro, K., Nishii, R., Sawazaki, I., Sofuku, T., Fuchigami, T., Sudo, H., Effendi, N., Makino, A., Kiyono, Y., Shiba, K., et al. (2022). Development of Radiohalogenated Osimertinib Derivatives as Imaging Probes for Companion Diagnostics of Osimertinib. *J. Med. Chem.* 65, 1835–1847. <https://doi.org/10.1021/acs.jmedchem.1c01211>.
40. Goos, J.A.C.M., Cho, A., Carter, L.M., Dilling, T.R., Davydova, M., Mandleywala, K., Puttick, S., Gupta, A., Price, W.S., Quinn, J.F., et al. (2020). Delivery of polymeric nanostars for molecular imaging and endoradiotherapy through the enhanced

- permeability and retention (EPR) effect. *Theranostics* 10, 567–584. <https://doi.org/10.7150/thno.36777>.
41. Banerjee, S.R., Foss, C.A., Horhota, A., Pullambhatla, M., McDonnell, K., Zale, S., and Pomper, M.G. (2017). (111)In- and IRDye800CW-Labeled PLA-PEG Nanoparticle for Imaging Prostate-Specific Membrane Antigen-Expressing Tissues. *Biomacromolecules* 18, 201–209. <https://doi.org/10.1021/acs.biomac.6b01485>.
 42. Zhong, X., Guo, J., Han, X., Wu, W., Yang, R., Zhang, J., and Shao, G. (2023). Synthesis and Preclinical Evaluation of a Novel FAPI-04 Dimer for Cancer Theranostics. *Mol. Pharm.* 20, 2402–2414. <https://doi.org/10.1021/acs.molpharmaceut.2c00965>.
 43. Bozkurt, M.F., Virgolini, I., Balogova, S., Beheshti, M., Rubello, D., Decristoforo, C., Ambrosini, V., Kjaer, A., Delgado-Bolton, R., Kunikowska, J., et al. (2017). Guideline for PET/CT imaging of neuroendocrine neoplasms with (68)Ga-DOTA-conjugated somatostatin receptor targeting peptides and (18)F-DOPA. *Eur. J. Nucl. Med. Mol. Imag.* 44, 1588–1601. <https://doi.org/10.1007/s00259-017-3728-y>.
 44. Luining, W.I., Cysouw, M.C.F., Meijer, D., Hendrikse, N.H., Boellaard, R., Vis, A.N., and Oprea-Lager, D.E. (2022). Targeting PSMA Revolutionizes the Role of Nuclear Medicine in Diagnosis and Treatment of Prostate Cancer. *Cancers* 14, 1169. <https://doi.org/10.3390/cancers14051169>.
 45. van Schooneveld, M.M., Cormode, D.P., Koole, R., van Wijngaarden, J.T., Calcagno, C., Skajaa, T., Hilhorst, J., 't Hart, D.C., Fayad, Z.A., Mulder, W.J.M., and Meijerink, A. (2010). A fluorescent, paramagnetic and PEGylated gold/silica nanoparticle for MRI, CT and fluorescence imaging. *Contrast Media Mol. Imaging* 5, 231–236. <https://doi.org/10.1002/cmmi.376>.
 46. Regino, C.A.S., Walbridge, S., Bernardo, M., Wong, K.J., Johnson, D., Lonser, R., Oldfield, E.H., Choyke, P.L., and Brechbiel, M.W. (2008). A dual CT-MR dendrimer contrast agent as a surrogate marker for convection-enhanced delivery of intracerebral macromolecular therapeutic agents. *Contrast Media Mol. Imaging* 3, 2–8. <https://doi.org/10.1002/cmmi.223>.
 47. Ashton, J.R., Clark, D.P., Moding, E.J., Ghaghada, K., Kirsch, D.G., West, J.L., and Badea, C.T. (2014). Dual-Energy Micro-CT Functional Imaging of Primary Lung Cancer in Mice Using Gold and Iodine Nanoparticle Contrast Agents: A Validation Study. *PLoS One* 9, e88129. <https://doi.org/10.1371/journal.pone.0088129>.
 48. Rabin, O., Manuel Perez, J., Grimm, J., Wojtkiewicz, G., and Weissleder, R. (2006). An X-ray computed tomography imaging agent based on long-circulating bismuth sulphide nanoparticles. *Nat. Mater.* 5, 118–122. <https://doi.org/10.1038/nmat1571>.
 49. Pan, D., Schirra, C.O., Senpan, A., Schmieder, A.H., Stacy, A.J., Roessl, E., Thran, A., Wickline, S.A., Proskia, R., and Lanza, G.M. (2012). An Early Investigation of Ytterbium Nanocolloids for Selective and Quantitative “Multicolor” Spectral CT Imaging. *ACS Nano* 6, 3364–3370. <https://doi.org/10.1021/nn300392x>.
 50. Toczek, J., Boodagh, P., Sanzida, N., Ghim, M., Salarian, M., Gona, K., Kukreja, G., Rajendran, S., Wei, L., Han, J., et al. (2021). Computed tomography imaging of macrophage phagocytic activity in abdominal aortic aneurysm. *Theranostics* 11, 5876–5888. <https://doi.org/10.7150/thno.55106>.
 51. Ohgushi, M., Nagayama, K., and Wada, A. (1969). Dextran-magnetite: A new relaxation reagent and its application to T2 measurements in gel systems. *J. Magn. Reson.* 29, 599–601. [https://doi.org/10.1016/0022-2364\(78\)90018-5](https://doi.org/10.1016/0022-2364(78)90018-5).
 52. Miller, M.A., Gadde, S., Pfirschke, C., Engblom, C., Sprachman, M.M., Kohler, R.H., Yang, K.S., Laughney, A.M., Wojtkiewicz, G., Kamaly, N., et al. (2015). Predicting therapeutic nanomedicine efficacy using a companion magnetic resonance imaging nanoparticle. *Sci. Transl. Med.* 7, 314ra183. <https://doi.org/10.1126/scitranslmed.aac6522>.
 53. Ponce, A.M., Viglianti, B.L., Yu, D., Yarmolenko, P.S., Michelich, C.R., Woo, J., Bally, M.B., and Dewhurst, M.W. (2007). Magnetic resonance imaging of temperature-sensitive liposome release: drug dose painting and antitumor effects. *J. Natl. Cancer Inst.* 99, 53–63. <https://doi.org/10.1093/jnci/djk005>.
 54. van Elk, M., Lorenzato, C., Ozbakir, B., Oerlemans, C., Storm, G., Nijsen, F., Deckers, R., Vermonden, T., and Hennink, W.E. (2015). Alginate microgels loaded with temperature sensitive liposomes for magnetic resonance imageable drug release and microgel visualization. *Eur. Polym. J.* 72, 620–631. <https://doi.org/10.1016/j.eurpolymj.2015.03.013>.
 55. Guan, G., Zhang, C., Liu, H., Wang, Y., Dong, Z., Lu, C., Nan, B., Yue, R., Yin, X., Zhang, X.-B., and Song, G. (2022). Ternary Alloy PtWm as a Mn Nanoreservoir for High-Field MRI Monitoring and Highly Selective Ferroptosis Therapy. *Angew Chem. Int. Ed. Engl.* 61, e202117229. <https://doi.org/10.1002/anie.202117229>.
 56. Yue, R., Zhang, C., Xu, L., Wang, Y., Guan, G., Lei, L., Zhang, X., and Song, G. (2022). Dual key co-activated nanoplatfor for switchable MRI monitoring accurate ferroptosis-based synergistic therapy. *Chem* 8, 1956–1981. <https://doi.org/10.1016/j.chempr.2022.03.009>.
 57. Shi, L., Wang, Y., Zhang, C., Zhao, Y., Lu, C., Yin, B., Yang, Y., Gong, X., Teng, L., Liu, Y., et al. (2021). An Acidity-Unlocked Magnetic Nanoplatfor Enables Self-Boosting ROS Generation through Upregulation of Lactate for Imaging-Guided Highly Specific Chemodynamic Therapy. *Angew Chem. Int. Ed. Engl.* 60, 9562–9572. <https://doi.org/10.1002/anie.202014415>.
 58. Liu, M., Guo, X., Wang, S., Jin, M., Wang, Y., Li, J., and Liu, J. (2013). BOLD-MRI of breast invasive ductal carcinoma: correlation of R2* value and the expression of HIF-1alpha. *Eur. Radiol.* 23, 3221–3227. <https://doi.org/10.1007/s00330-013-2937-4>.
 59. Tóth, V., Förschler, A., Hirsch, N.M., den Hollander, J., Kooijman, H., Gempt, J., Ringel, F., Schlegel, J., Zimmer, C., and Preibisch, C. (2013). MR-based hypoxia measures in human glioma. *J. Neuro Oncol.* 115, 197–207. <https://doi.org/10.1007/s11060-013-1210-7>.
 60. Xie, C., Cen, D., Ren, Z., Wang, Y., Wu, Y., Li, X., Han, G., and Cai, X. (2020). FeS@BSA Nanoclusters to Enable H(2)S-Amplified ROS-Based Therapy with MRI Guidance. *Adv. Sci.* 7, 1903512. <https://doi.org/10.1002/advs.201903512>.
 61. Li, M., Huo, L., Zeng, J., Zhu, G., Liu, X., Zhu, X., Huang, G., Wang, Y., Ni, K., and Zhao, Z. (2023). Switchable ROS Scavenger/Generator for MRI-Guided Anti-Inflammation and Anti-Tumor Therapy with Enhanced Therapeutic Efficacy and Reduced Side Effects. *Adv. Healthc. Mater.* 12, e2202043. <https://doi.org/10.1002/adhm.202202043>.
 62. Zhang, C., Li, J., Lu, C., Yang, T., Zhao, Y., Teng, L., Yang, Y., Song, G., and Zhang, X.-B. (2021). H2S-Activated “One-Key Triple-Lock” Bis-Metal Coordination Network for Visualizing Precise Therapy of Colon Cancer. *CCS Chem.* 3, 2126–2142. <https://doi.org/10.31635/ccschem.020.202000369>.
 63. Naumenko, V.A., Vodopyanov, S.S., Vlasova, K.Y., Potashnikova, D.M., Melnikov, P.A., Vishnevskiy, D.A., Garanina, A.S., Valikhov, M.P., Lipatova, A.V., Chekhonin, V.P., et al. (2021). Intravital imaging of liposome behavior upon repeated administration: A step towards the development of liposomal companion diagnostic for cancer nanotherapy. *J. Contr. Release* 330, 244–256. <https://doi.org/10.1016/j.jconrel.2020.12.014>.
 64. Dong, X., Yin, W., Yu, J., Dou, R., Bao, T., Zhang, X., Yan, L., Yong, Y., Su, C., Wang, Q., et al. (2016). Mesoporous Bamboo Charcoal Nanoparticles as a New Near-Infrared Responsive Drug Carrier for Imaging-Guided Chemotherapy/Photothermal Synergistic Therapy of Tumor. *Adv. Healthc. Mater.* 5, 1627–1637. <https://doi.org/10.1002/adhm.201600287>.
 65. Zhu, H., Ren, F., Wang, T., Jiang, Z., Sun, Q., and Li, Z. (2022). Targeted Immunoinaging of Tumor-Associated Macrophages in Orthotopic Glioblastoma by the NIR-IIb Nanoprob. *Small* 18, e2202201. <https://doi.org/10.1002/smll.202202201>.
 66. Ma, Y., Xu, L., Yin, B., Shang, J., Chen, F., Xu, J., Song, Z.L., Nan, B., Song, G., and Zhang, X.B. (2021). Ratiometric Semiconducting Polymer Nanoparticle for Reliable Photoacoustic Imaging of Pneumonia-Induced Vulnerable Atherosclerotic Plaque in Vivo. *Nano Lett.* 21, 4484–4493. <https://doi.org/10.1021/acs.nanolett.1c01359>.

67. Yin, B., Wang, Y., Zhang, C., Zhao, Y., Wang, Y., Teng, L., Yang, Y., Zeng, Z., Huan, S., Song, G., and Zhang, X. (2019). Oxygen-Embedded Quinoidal Acene Based Semiconducting Chromophore Nanoprobe for Amplified Photoacoustic Imaging and Photothermal Therapy. *Anal. Chem.* 91, 15275–15283. <https://doi.org/10.1021/acs.analchem.9b04429>.
68. Liu, Y., Teng, L., Yin, B., Meng, H., Yin, X., Huan, S., Song, G., and Zhang, X.B. (2022). Chemical Design of Activatable Photoacoustic Probes for Precise Biomedical Applications. *Chem. Rev.* 122, 6850–6918. <https://doi.org/10.1021/acs.chemrev.1c00875>.
69. Maji, S.K., Sreejith, S., Joseph, J., Lin, M., He, T., Tong, Y., Sun, H., Yu, S.W.-K., and Zhao, Y. (2014). Upconversion Nanoparticles as a Contrast Agent for Photoacoustic Imaging in Live Mice. *Adv. Mater.* 26, 5633–5638. <https://doi.org/10.1002/adma.201400831>.
70. Shashkov, E.V., Everts, M., Galanzha, E.I., and Zharov, V.P. (2008). Quantum Dots as Multimodal Photoacoustic and Photothermal Contrast Agents. *Nano Lett.* 8, 3953–3958. <https://doi.org/10.1021/nl802442x>.
71. Li, W., and Chen, X. (2015). Gold nanoparticles for photoacoustic imaging. *Nanomedicine* 10, 299–320. <https://doi.org/10.2217/nnm.14.169>.
72. Pu, K., Mei, J., Jokerst, J.V., Hong, G., Antaris, A.L., Chattopadhyay, N., Shuhendler, A.J., Kurosawa, T., Zhou, Y., Gambhir, S.S., et al. (2015). Diketopyrrolopyrrole-Based Semiconducting Polymer Nanoparticles for In Vivo Photoacoustic Imaging. *Adv. Mater.* 27, 5184–5190. <https://doi.org/10.1002/adma.201502285>.
73. Teng, L., Han, X., Liu, Y., Lu, C., Yin, B., Huan, S., Yin, X., Zhang, X.-B., and Song, G. (2021). Smart Nanozyme Platform with Activity-Related Ratiometric Molecular Imaging for Predicting Therapeutic Effects. *Angew Chem. Int. Ed. Engl.* 60, 26142–26150. <https://doi.org/10.1002/anie.202110427>.
74. Poon, W., Heinmiller, A., Zhang, X., and Nadeau, J.L. (2015). Determination of biodistribution of ultrasmall, near-infrared emitting gold nanoparticles by photoacoustic and fluorescence imaging. *J. Biomed. Opt.* 20, 066007. <https://doi.org/10.1117/1.JBO.20.6.066007>.
75. Spence, T., De Souza, R., Dou, Y., Stapleton, S., Reilly, R.M., and Allen, C. (2015). Integration of imaging into clinical practice to assess the delivery and performance of macromolecular and nanotechnology-based oncology therapies. *J. Contr. Release* 219, 295–312. <https://doi.org/10.1016/j.jconrel.2015.09.036>.
76. Bam, R., Lown, P.S., Stern, L.A., Sharma, K., Wilson, K.E., Bean, G.R., Lutz, A.M., Paulmurugan, R., Hackel, B.J., Dahl, J., and Abou-Elkacem, L. (2020). Efficacy of Affibody-Based Ultrasound Molecular Imaging of Vascular B7-H3 for Breast Cancer Detection. *Clin. Cancer Res.* 26, 2140–2150. <https://doi.org/10.1158/1078-0432.CCR-19-1655>.
77. Köse, G., Darguzyte, M., and Kiessling, F. (2020). Molecular Ultrasound Imaging. *Nanomaterials* 10, 1935. <https://doi.org/10.3390/nano10101935>.
78. Wischhusen, J., Wilson, K.E., Delcros, J.G., Molina-Peña, R., Gibert, B., Jiang, S., Ngo, J., Goldschneider, D., Mehlen, P., Willmann, J.K., and Padilla, F. (2018). Ultrasound molecular imaging as a non-invasive companion diagnostic for netrin-1 interference therapy in breast cancer. *Theranostics* 8, 5126–5142. <https://doi.org/10.7150/thno.27221>.
79. Lucero, M.Y., and Chan, J. (2021). Photoacoustic imaging of elevated glutathione in models of lung cancer for companion diagnostic applications. *Nat. Chem.* 13, 1248–1256. <https://doi.org/10.1038/s41557-021-00804-0>.
80. Ishimoto, Y., Tanaka, T., Yoshida, Y., and Inagi, R. (2018). Physiological and pathophysiological role of reactive oxygen species and reactive nitrogen species in the kidney. *Clin. Exp. Pharmacol. Physiol.* 45, 1097–1105. <https://doi.org/10.1111/1440-1681.13018>.
81. Wang, Y., Shi, L., Ye, Z., Guan, K., Teng, L., Wu, J., Yin, X., Song, G., and Zhang, X.B. (2020). Reactive Oxygen Correlated Chemiluminescent Imaging of a Semiconducting Polymer Nanoplatfor for Monitoring Chemodynamic Therapy. *Nano Lett.* 20, 176–183. <https://doi.org/10.1021/acs.nanolett.9b03556>.
82. Chen, T., Chen, Z., Zhou, Q., Ding, H., Gong, P., Wang, J., Cai, H., Ao, R., Yu, M., Song, J., et al. (2022). Microenvironment-Tailored Catalytic Nanoprobe for Ratiometric NIR-II Fluorescence/Photoacoustic Imaging of H₂O₂ in Tumor and Lymphatic Metastasis. *Adv. Funct. Mater.* 32, 2208720. <https://doi.org/10.1002/adfm.202208720>.
83. Liu, P., Jin, Y., Sattar, H., Liu, H., Xie, W., and Zhou, F. (2018). Natural killer cell immunotherapy against multiple myeloma: Progress and possibilities. *J. Leukoc. Biol.* 103, 821–828. <https://doi.org/10.1002/JLB.2RU0517-176RR>.
84. Chiossone, L., Dumas, P.-Y., Vienne, M., and Vivier, E. (2018). Natural killer cells and other innate lymphoid cells in cancer. *Nat. Rev. Immunol.* 18, 671–688. <https://doi.org/10.1038/s41577-018-0061-z>.
85. Shaffer, T.M., Aalipour, A., Schürch, C.M., and Gambhir, S.S. (2020). PET Imaging of the Natural Killer Cell Activation Receptor NKp30. *J. Nucl. Med.* 61, 1348–1354. <https://doi.org/10.2967/jnumed.119.233163>.
86. Weist, M.R., Starr, R., Aguilar, B., Chea, J., Miles, J.K., Poku, E., Gerds, E., Yang, X., Priceman, S.J., Forman, S.J., et al. (2018). PET of Adoptively Transferred Chimeric Antigen Receptor T Cells with ⁸⁹Zr-Oxine. *J. Nucl. Med.* 59, 1531–1537. <https://doi.org/10.2967/jnumed.117.206714>.
87. Zhao, H., Wang, C., Yang, Y., Sun, Y., Wei, W., Wang, C., Wan, L., Zhu, C., Li, L., Huang, G., and Liu, J. (2021). ImmunoPET imaging of human CD8(+) T cells with novel (68)Ga-labeled nanobody companion diagnostic agents. *J. Nanobiotechnol.* 19, 42. <https://doi.org/10.1186/s12951-021-00785-9>.
88. Mantovani, A., Sozzani, S., Locati, M., Allavena, P., and Sica, A. (2002). Macrophage polarization: tumor-associated macrophages as a paradigm for polarized M2 mononuclear phagocytes. *Trends Immunol.* 23, 549–555. [https://doi.org/10.1016/S1471-4906\(02\)02302-5](https://doi.org/10.1016/S1471-4906(02)02302-5).
89. Yuan, P., Xu, X., Hu, D., Chen, Y., Fan, J., Yao, S., Piao, Y., Zhou, Z., Shao, S., Slater, N.K.H., et al. (2023). Highly Sensitive Imaging of Tumor Metastasis Based on the Targeting and Polarization of M2-like Macrophages. *J. Am. Chem. Soc.* 145, 7941–7951. <https://doi.org/10.1021/jacs.2c13218>.
90. Ruiz de Garibay, G., García de Jalón, E., Stigen, E., Lund, K.B., Popa, M., Davidson, B., Safont, M.M., Rygh, C.B., Espedal, H., Barrett, T.M., et al. (2021). Repurposing (18)F-FMISO as a PET tracer for translational imaging of nitroreductase-based gene directed enzyme prodrug therapy. *Theranostics* 11, 6044–6057. <https://doi.org/10.7150/thno.55092>.
91. Arlauckas, S.P., Popov, A.V., and Delikatny, E.J. (2014). Direct inhibition of choline kinase by a near-infrared fluorescent carbocyanine. *Mol. Cancer Therapeut.* 13, 2149–2158. <https://doi.org/10.1158/1535-7163.MCT-14-0085>.
92. Arlauckas, S.P., Kumar, M., Popov, A.V., Poptani, H., and Delikatny, E.J. (2017). Near infrared fluorescent imaging of choline kinase alpha expression and inhibition in breast tumors. *Oncotarget* 8, 16518–16530.
93. Asano, T., Nagayo, Y., Tsuda, S., Ito, A., Kobayashi, W., Fujita, K., Sato, K., Nishiguchi, K.M., Kunikata, H., Fujioka, H., et al. (2020). Companion Diagnosis for Retinal Neuroprotective Treatment by Real-Time Imaging of Calpain Activation Using a Novel Fluorescent Probe. *Bioconjugate Chem.* 31, 2241–2251. <https://doi.org/10.1021/acs.bioconjchem.0c00435>.
94. Gniadek, T.J., Li, Q.K., Tully, E., Chatterjee, S., Nimmagadda, S., and Gabrielson, E. (2017). Heterogeneous expression of PD-L1 in pulmonary squamous cell carcinoma and adenocarcinoma: implications for assessment by small biopsy. *Mod. Pathol.* 30, 530–538. <https://doi.org/10.1038/modpathol.2016.213>.
95. Bensch, F., van der Veen, E.L., Lub-de Hooge, M.N., Jorritsma-Smit, A., Boellaard, R., Kok, I.C., Oosting, S.F., Schröder, C.P., Hiltermann, T.J.N., van der Wekken, A.J., et al. (2018). (89)Zr-atezolizumab imaging as a non-invasive approach to assess clinical response to PD-L1 blockade in cancer. *Nat. Med.* 24, 1852–1858. <https://doi.org/10.1038/s41591-018-0255-8>.
96. Ou, Y.C., Wen, X., Johnson, C.A., Shae, D., Ayala, O.D., Webb, J.A., Lin, E.C., DeLapp, R.C., Boyd, K.L., Richmond, A., et al. (2020).

- Multimodal Multiplexed Immunoimaging with Nanostars to Detect Multiple Immunomarkers and Monitor Response to Immunotherapies. *ACS Nano* 14, 651–663. <https://doi.org/10.1021/acsnano.9b07326>.
97. Wang, Y., Hu, X., Weng, J., Li, J., Fan, Q., Zhang, Y., and Ye, D. (2019). A Photoacoustic Probe for the Imaging of Tumor Apoptosis by Caspase-Mediated Macrocyclization and Self-Assembly. *Angew Chem. Int. Ed. Engl.* 58, 4886–4890. <https://doi.org/10.1002/anie.201813748>.
98. Honold, L., Austrup, M., Faust, A., Konken, C.P., Schwegmann, K., Zinnhardt, B., Daniliuc, C.G., Haufe, G., Schäfers, M., Kopka, K., and Hermann, S. (2022). Towards Optimized Bioavailability of (99m)Tc-Labeled Barbiturates for Non-invasive Imaging of Matrix Metalloproteinase Activity. *Mol. Imag. Biol.* 24, 434–443. <https://doi.org/10.1007/s11307-021-01668-z>.
99. Torelli, M.D., Rickard, A.G., Backer, M.V., Filonov, D.S., Nunn, N.A., Kinev, A.V., Backer, J.M., Palmer, G.M., and Shenderova, O.A. (2019). Targeting Fluorescent Nanodiamonds to Vascular Endothelial Growth Factor Receptors in Tumor. *Bioconjugate Chem.* 30, 604–613. <https://doi.org/10.1021/acs.bioconjchem.8b00803>.
100. Yin, B., Qin, Q., Li, Z., Wang, Y., Liu, X., Liu, Y., Huan, S., Zhang, X., and Song, G. (2022). Tongue cancer tailored photosensitizers for NIR-II fluorescence imaging guided precise treatment. *Nano Today* 45, 101550. <https://doi.org/10.1016/j.nantod.2022.101550>.
101. Graf, T.P., Qiu, S.Y., Varshney, D., Laracuate, M.L., Euliano, E.M., Munnangi, P., Pogostin, B.H., Baryakova, T., Garyali, A., and McHugh, K.J. (2023). A Scalable Platform for Fabricating Biodegradable Microparticles with Pulsatile Drug Release. *Advanced Materials*, e2300228. <https://doi.org/10.1002/adma.202300228>.
102. Wang, Y., Song, G., Liao, S., Qin, Q., Zhao, Y., Shi, L., Guan, K., Gong, X., Wang, P., Yin, X., et al. (2021). Cyclic Amplification of the Afterglow Luminescent Nanoreporter Enables the Prediction of Anti-cancer Efficiency. *Angew Chem. Int. Ed. Engl.* 60, 19779–19789. <https://doi.org/10.1002/anie.202104127>.
103. Liao, S., Wang, Y., Li, Z., Zhang, Y., Yin, X., Huan, S., Zhang, X.B., Liu, S., and Song, G. (2022). A novel afterglow nanoreporter for monitoring cancer therapy. *Theranostics* 12, 6883–6897. <https://doi.org/10.7150/thno.77457>.
104. Liu, H., Lu, C., Han, L., Zhang, X., and Song, G. (2021). Optical – Magnetic probe for evaluating cancer therapy. *Coord. Chem. Rev.* 441, 213978. <https://doi.org/10.1016/j.ccr.2021.213978>.
105. Song, G., Kenney, M., Chen, Y.S., Zheng, X., Deng, Y., Chen, Z., Wang, S.X., Gambhir, S.S., Dai, H., and Rao, J. (2020). Carbon-coated FeCo nanoparticles as sensitive magnetic-particle-imaging tracers with photothermal and magnetothermal properties. *Nat. Biomed. Eng.* 4, 325–334. <https://doi.org/10.1038/s41551-019-0506-0>.
106. Farzin, A., Etesami, S.A., Quint, J., Memic, A., and Tamayol, A. (2020). Magnetic Nanoparticles in Cancer Therapy and Diagnosis. *Adv. Healthc. Mater.* 9, e1901058. <https://doi.org/10.1002/adhm.201901058>.